Available online at www.sciencedirect.com
SCIENCE DIRECT®
Journal of Sound and Vibration 277 (2004) 711–739
JOURNAL OF SOUND AND VIBRATION
www.elsevier.com/locate/jsvi

# Structural non-linearities and the nature of the classic flutter instability

B.D. Coller[a,*], P.A. Chamara[b]

[a] Department of Mechanical Engineering, Northern Illinois University, DeKalb, IL 60115, USA
[b] Department of Mechanical Engineering, University of Illinois at Chicago, Chicago, IL 60607-7022, USA

Received 6 September 2001; accepted 4 September 2003

**Abstract**

The paper presents an investigation of the subcritical/supercritical nature of the flutter Hopf bifurcation of a two degree of freedom with linear, quadratic, and cubic restoring forces. Under certain conditions, the instability gives rise to stable limit cycle oscillations, whereas unstable periodic orbits appear for other conditions, providing a potentially dangerous non-linear instability mechanism in regimes for which linear analyses predict stability. The analytic approach employed herein, allows for a more thorough investigation of the high-dimensional parameter space than that afforded by others' experimental and computational efforts. Counterexamples to previously held conjectures are readily found. Favorable comparisons are made to predictions based on less rigorous describing function or harmonic balance techniques.


## 1. Introduction

It has been nearly three quarters of a century since Theodorsen's seminal linear analysis illuminating the physical mechanism of airfoil flutter. Mathematically, the self-excited instability corresponds to a complex conjugate pair of eigenvalues crossing the imaginary axis transversely, a *Hopf Bifurcation*. While linear analyses suffice to determine stability conditions with respect to infinitesimal perturbations, they provide no information of the interesting and potentially destabilizing non-linear phenomena that may occur even for reasonably small motions.

Hopf's theorem [1] leads us to generically expect the change in stability to spawn limit cycle oscillations. The instabilities typically come in two forms: supercritical or subcritical. The former gives rise to stable periodic orbits on the unstable side of the instability, providing a dynamic

*Corresponding author. Tel.: +1-815-753-9944; fax: +1-815-753-0146.
*E-mail address:* coller@ceet.niu.edu (B.D. Coller).

0022-460X/$ - see front matter 
doi:10.1016/j.jsv.2003.09.017

mechanism that arrests post-instability growth of solutions. Subcritical Hopf bifurcations, on the other hand, produce unstable periodic orbits within regimes for which a linear analysis predicts the aeroelastic system is stable. Under such conditions, small perturbations of the state could lead to catastrophic growing oscillations even though the classical Theodorsen analysis predicts stability. In the present paper, we outline a procedure for efficiently performing parametric studies to determine the conditions which lead to subcritical and supercritical bifurcations in the classical flutter problem with non-linear structural restoring forces. It is a task of particular importance to us. Currently, we are considering using fluttering airfoils as passive actuators in a class of flow control problems.

We are far from the first to perform parametric studies of the non-linear character of the flutter instability. Woolston [2], in 1957, simulated the equations of motion on an analog computer. More recently, Lee et al. [3] embarked on a limit cycle safari, using numerical integration of a model set of equations and perturbation theory to determine supercritical and subcritical regimes, amplitudes, and frequencies of oscillation. Several authors (e.g., Refs. [4–9]) have investigated the non-linear dynamics well beyond the flutter instability, cataloging secondary bifurcations, period doublings, and chaos in a handful of representative systems.

In the classical linear flutter problem, there are six dimensionless parameters that characterize the dynamical system. Additional parameters are needed to characterize non-linearities in the restoring springs. The rather high dimension of parameter space leads Lee et al. [3] to state that "a complete parametric study of the system [would be] practically impossible." As a consequence, previous researchers performing physical and numerical experiments have considered a severely restricted set of test cases, often only considering variations of a single-parameter cubic non-linearity in the restoring torque of the pitch spring. Nonetheless, they have inferred a general principle [2,3]: when the pitch spring is hard (i.e., stiffness increases with deflection), the Hopf bifurcation is of the more benign supercritical variety, and when the spring is soft (opposite of hard), one encounters the more dangerous subcritical Hopf bifurcations. We shall refer to this empirical principle as the "flutter criticality hypothesis." Although previous authors acknowledge that counterexamples may exist, and even offer hypothetical physical mechanisms [2,3], we are unaware of any such counterexamples demonstrated in the literature. Price et al. [4] claim to discover limit cycle oscillations at flow speeds below the linear flutter boundary in a system with a hard pitch spring. However, a closer examination of their work reveals what we would consider an improper calculation of the linear flutter velocity: if one properly linearizes the system about the undeflected equilibrium, one obtains a supercritical Hopf bifurcation in accordance with the flutter criticality hypothesis.

In the current work, we seek an analytical approach to avoid laborious searches via numerical simulation and experiment. Ignoring, for the moment, secondary instabilities, period doublings and chaos, we focus here on the subcritical/supercritical nature of the primary flutter instability. Although describing function (harmonic balance) analyses have been successfully implemented in flutter problems [10–12,4], we initially shy away from the technique. Strong filtering assumptions, on which the describing function techniques rely, do not apply to the flutter problem, and we are skeptical about its lack of rigor. Instead, we employ the theories of center manifolds and normal forms. Through a short sequence of algebraic manipulations, we are able to calculate a normal form coefficient, the sign of which determines whether the bifurcation is subcritical or supercritical. The ease at which we can perform the calculation affords a more thorough

investigation of the parameter space through which we readily find counterexamples to the flutter criticality hypothesis. Furthermore, we note that the theoretical framework developed here serves as a foundation upon which we build analyses of the considerably richer dynamics of multiple blade [13,14] and cascade flutter.

During the final stage of preparation of this manuscript, we learned of work by Liu et al. [15] in which center manifolds and normal forms were used to study the same physical system. However, the research objectives of that paper differ markedly from ours, and the two projects complement each other.

Finally, since our analyses are performed on reduced order models, we back up our findings via numerical simulations of a high fidelity model with linearized aerodynamics.

## 2. Low order dynamical model

### 2.1. Model development

The dynamical systems analysis tools that we seek to apply to the fluid–structure interaction problem require that, unlike traditional flutter analyses, we represent the system as a relatively small set of ordinary differential equations (ODEs) in the time domain. A schematic of the canonical flutter problem is depicted in Fig. 1. The airfoil, situated in a 2-D incompressible, inviscid, and nominally irrotational flow, has two elastic degrees of freedom: vertical translation (plunge), and rotation (twist) about some pre-defined elastic axis. The equations of motion for the system, after scaling become

$$\begin{aligned} &\tilde{h}'' - \chi\cos(\alpha)\alpha'' + \chi\sin(\alpha)\alpha'^2 + r_\alpha^2\frac{\partial\tilde{V}}{\partial\tilde{h}} = \frac{\tilde{U}^2}{\mu}\tilde{L},\\ &-\chi\cos(\alpha)\tilde{h}'' + r_\alpha^2\alpha'' + r_\alpha^2\frac{\partial\tilde{V}}{\partial\alpha} = \frac{\tilde{U}^2}{\mu}\tilde{M}_{ea}, \end{aligned} \tag{1}$$

where $\tilde{L}$ and $\tilde{M}_{ea}$ are the non-dimensional lift and aerodynamic pitching moment about the elastic axis, respectively. The astute reader will note two main differences between the equations above and those that typically appear in the flutter literature. The first is cosmetic due to our preference to call upward displacements positive. Secondly, rather than scale time by the flow speed as is customary, we scale time $t$ by the uncoupled natural pitch frequency: $\tau = \sqrt{k_{\alpha 1}/I_{ea}}t = \omega_\alpha t$. This mechanical scaling allows us to consider flow regimes which include $U = 0$ without any special

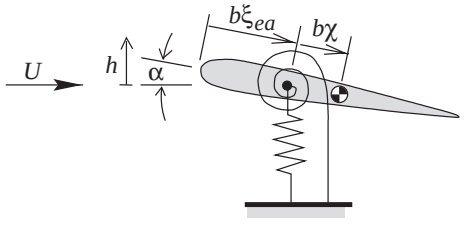


Fig. 1. Schematic of the physical system.

effort. The symbol $\tilde{V}$ above represents the potential for the elastic restoring forces:

$$\tilde{V} = \frac{X^2}{r_\alpha^2}\left[\tfrac{1}{2}\tilde{h}^2 + \tfrac{1}{3}\delta_{h_2}\tilde{h}^3 + \tfrac{1}{4}\delta_{h_3}\tilde{h}^4\right] + \tfrac{1}{2}\alpha^2 + \tfrac{1}{3}\delta_{\alpha_2}\alpha^3 + \tfrac{1}{4}\delta_{\alpha_3}\alpha^4. \tag{2}$$

Thus, we consider independent pitch and plunge springs with quadratic and cubic non-linearities.

In the discussion that follows, we assume that the structural non-linearities are more severe that those due to the aerodynamics. Thus the incidence angles are safely under $10^\circ$ and we may apply small angle approximations $\cos(\alpha)\approx 1$, $\sin(\alpha)\alpha'^2 \approx 0$, and the inertial non-linearities in Eq. (1) vanish. Under these conditions, the unsteady aerodynamic lift and moment are well approximated by

$$\tilde{L}(\tau) = \frac{L}{\pi\rho b U^2} = 2\tilde{G}(\tau) - \frac{1}{\tilde{U}^2}h''(\tau) + \frac{1}{\tilde{U}}\alpha'(\tau) - \frac{\xi_{ea}-1}{\tilde{U}^2}\alpha''(\tau) \tag{3}$$

and

$$\tilde{M}_{ea}(\tau) = \frac{M_{ea}}{\pi\rho b^2 U^2} = 2\left(\xi_{ea}-\tfrac{1}{2}\right)\tilde{G}(\tau) + \frac{\xi_{ea}-1}{\tilde{U}^2}[-\tilde{h}'' - (\xi_{ea}-1)\alpha''] + \frac{\xi_{ea}-\frac{3}{2}}{\tilde{U}}\alpha' - \frac{1}{8\tilde{U}^2}\alpha''. \tag{4}$$

The first term in each of these expressions contains

$$\tilde{G}(\tau) = \Phi(\tilde{U}\tau)\tilde{W}_{3/4}(0) + \int_0^\tau \Phi(\tilde{U}(\tau-\tau_0))\frac{\mathrm{d}\tilde{W}_{3/4}}{\mathrm{d}\tau_0}\,\mathrm{d}\tau_0, \tag{5}$$

where $\Phi$ is Wagner's function. The scale factor $\tilde{U}$ in its argument maps the "mechanical" non-dimensional time, $\tau = \omega_\alpha t$ to "aerodynamic" non-dimensional time $\hat{\tau} = Ut/b$, (i.e., $\hat{\tau} = U\tau/\omega_\alpha b = \tilde{U}\tau$) with which Wagner's function is usually defined. The symbol $\tilde{W}_{3/4}$ in Eq. (5) is the normalized upwash at the $\frac{3}{4}$- chord location on the flat plate airfoil due to its angle of incidence and motion:

$$\tilde{W}_{3/4} = \frac{W_{3/4}}{U} = -\frac{1}{\tilde{U}}\tilde{h}' + \alpha + \frac{1}{\tilde{U}}\left(\tfrac{3}{2}-\xi_{ea}\right)\alpha'. \tag{6}$$

The remaining terms in Eqs. (3) and (4) come from apparent mass effects and what Fung [16] calls a circulatory centrifugal force.

Performing integration by parts on Eq. (5), we obtain

$$\tilde{G}(\tau) = \Phi(0)\tilde{W}_{3/4}(\tau) - \int_0^\tau \frac{\partial\Phi(\tilde{U}(\tau-\tau_0))}{\partial\tau_0}W_{3/4}(\tau_0)\,\mathrm{d}\tau_0.$$

Although Wagner's function, $\Phi(\tau)$, is defined by integrating expressions containing products of modified Bessel functions, making the aerodynamics inherently infinite dimensional, Jones [17] and Jones [18] have devised good exponential approximations:

$$\Phi(\tilde{U}(\tau-\tau_0)) \approx 1 - K_2 e^{-\sigma_2\tilde{U}(\tau-\tau_0)} - K_3 e^{-\sigma_3\tilde{U}(\tau-\tau_0)}$$

$$\Rightarrow \quad \frac{\partial}{\partial\tau_0}\Phi(\tilde{U}(\tau-\tau_0)) \approx -\sigma_2\tilde{U}K_2 e^{-\sigma_2\tilde{U}(\tau-\tau_0)} - \sigma_3\tilde{U}K_3 e^{-\sigma_3\tilde{U}(\tau-\tau_0)}, \tag{7}$$

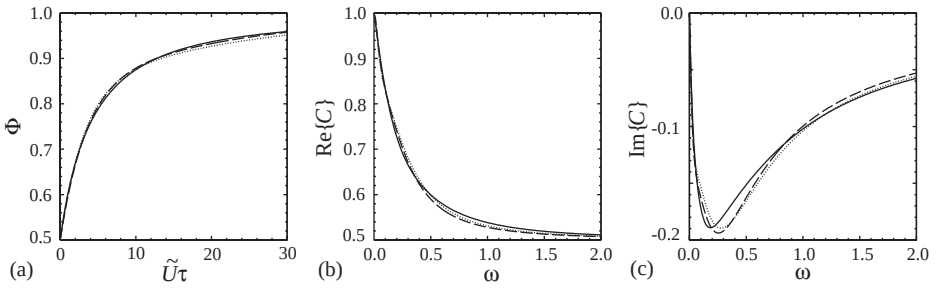


Fig. 2. Low order approximations to (a) Wagner's function, (b) the real part of Theodorsen's function, and (c) the imaginary part of Theodorsen's function. (Dashed), approximation using coefficients of Jones [17]; (dotted), approximation using coefficients of Jones [18]; (solid), true curves.

that can be effectively used to cast the unsteady aerodynamics in a low-dimensional setting (see Fig. 2(a)). Employing the approximation, Eq. (5) becomes

$$\tilde{G}(\tau) = \tilde{G}_0(\tau) + \tilde{G}_1(\tau) + \tilde{G}_2(\tau), \tag{8}$$

where

$$\tilde{G}_0(\tau) = (1 - K_1 - K_2)\tilde{W}_{3/4}(\tau), \tag{9}$$

$$\tilde{G}_j(\tau) = \sigma_j \tilde{U} K_j \int_0^\tau \mathrm{e}^{-\sigma_j \tilde{U}(\tau-\tau_0)} \tilde{W}_{3/4}(\tau_0)\,\mathrm{d}\tau_0, \quad j \in \{1,2\}. \tag{10}$$

We note that with the aid of Liebniz's rule,

$$\begin{aligned} \frac{\mathrm{d}}{\mathrm{d}\tau} G_j(\tau) &= -\sigma_j^2 \tilde{U}^2 K_j \int_0^\tau \tilde{W}_{3/4}(\tau_0)\,\mathrm{d}\tau_0 + \sigma_j \tilde{U} K_j W_{3/4}(\tau), \\ &= -\sigma_j \tilde{U}(\tilde{G}_j(\tau) - K_j W_{3/4}(\tau)). \end{aligned} \tag{11}$$

Thus by substituting Eqs. (8)–(11) into Eqs. (3) and (4), we express the unsteady aerodynamics in terms of two linear first order ordinary differential equations. Added to the two degree of freedom mechanical system (1), we obtain a set of equations on a six-dimensional phase space to describe the flow-induced vibrations. We believe the equations to be equivalent to the system of eight equations presented by Lee et al. [3], modified by a dimension-reducing simplification we have exploited.

### 2.2. Model validation

In Fig. 2(a), we show the approximations to Wagner's function (solid curve) using Eq. (7) and coefficients by Jones [17]: $K_1 = 0.165$, $\sigma_1 = 0.0455$, $K_2 = 0.335$, $\sigma_2 = 0.300$ (dashed curve); and Jones [18]: $K_1 = 0.165$, $\sigma_1 = 0.041$, $K_2 = 0.335$, $\sigma_2 = 0.32$ (dotted). It is a simple matter to calculate the complex frequency response of $G(\tau)$ to a sinusoidal input, $\tilde{W}_{3/4} = \mathrm{e}^{\mathrm{i}\omega\tilde{U}\tau}$. The result,

$$C(\omega) = \left[(1 - K_1 - K_2) + \frac{\sigma_1^2 K_1}{\sigma_1^2 + \omega^2} + \frac{\sigma_2^2 K_2}{\sigma_2^2 + \omega^2}\right] - \mathrm{i}\left[\frac{\sigma_1 K_1 \omega}{\sigma_1^2 + \omega^2} + \frac{\sigma_2 K_2 \omega}{\sigma_2^2 + \omega^2}\right], \tag{12}$$

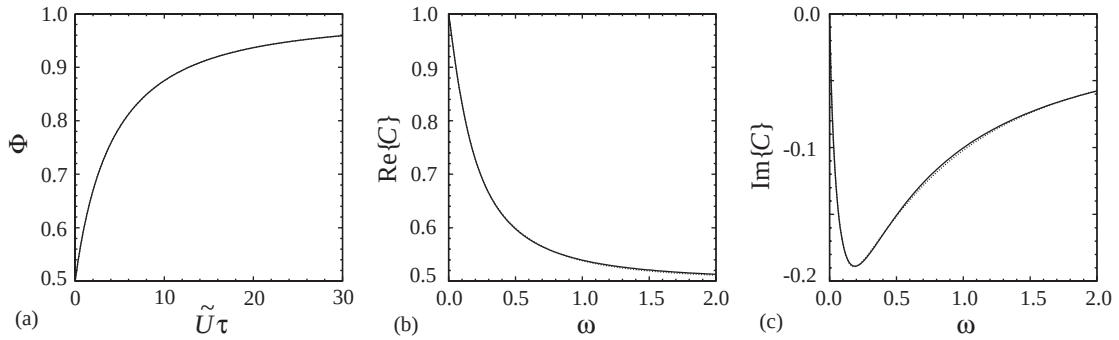


Fig. 3. Slightly higher order approximations to (a) Wagner's function, (b) the real part of Theodorsen's function, and (c) the imaginary part of Theodorsen's function. (Solid), the true functions, (dotted), approximations using fourth order aerodynamics.

is the analog of Theodorsen's function. In Figs. 2(b) and (c) we plot the real and imaginary parts of the approximate Theodorsen functions along with the true Theodorsen functions. We see that some of the differences between Wagner's function and its exponential approximations are amplified in the frequency response, particularly the imaginary parts.

With today's computers[1] it is a rather simple task to fit higher order approximations,

$$\Phi(\tilde{U}\tau) \approx 1 - \sum_{j=1}^{N_\Phi} K_j e^{-\sigma_j \tilde{U}\tau}, \tag{13}$$

to Wagner's function. Upon choosing $N_\Phi = 4$, we select $K_1 = 0.2552078488$, $\sigma_1 = 0.1708445093$, $K_2 = 0.1290432917$, $\sigma_2 = 0.5610424665$, $K_3 = 0.09654817188$, $\sigma_3 = 0.04680475392$, $K_4 = 0.01920068755$, $\sigma_4 = 0.006478169099$. Fig. 3 shows comparisons of the new aerodynamic model to Wagner's and Theodorsen's functions, similar to Fig. 2. This time, however, the approximations are nearly indistinguishable from the true step and frequency responses.

In Figs. 4(a) and (b), we show flutter speed, $\tilde{U}_F$, predictions for the six- and eight-dimensional models, respectively. The dotted curves in each of the figures represents the true flutter curves calculated by Theodorsen's flutter determinant [16]. Again, predictions of the model with fourth order aerodynamics agree almost exactly with those of the full system while those of the second order aerodynamics have more perceptible differences. Consequently, we shall use the eight-dimensional model with fourth order aerodynamics in the remainder of this investigation.

## 3. Dynamical systems toolbox

Oscillatory instabilities, whether occurring in models of flow-induced vibrations, electrical circuits, or chemical reactions, typically have the same mathematical structure. Here we briefly outline tools from the theory of non-linear dynamical systems we shall employ to distill, from the system, its essential features.

[1] Jones and Jones published their approximations in the 1940s.

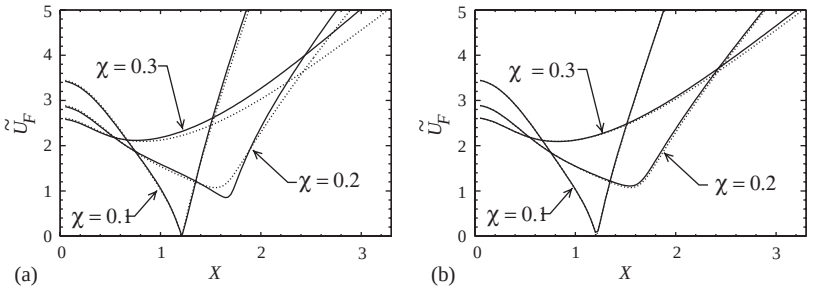


Fig. 4. Comparison of predicted flutter velocities, $\tilde{U}_F$, using (a) second order aerodynamic model; and (b) fourth order aerodynamic model. (Solid), approximate flutter boundaries computed with model; (dotted), actual flutter boundaries. System parameters: $r_a = 0.5$, $X = 1.7$, $\mu = 20.0$, $\xi_{ea} = 0.6$, and $\chi = 0.1$, 0.2, 0.3 as indicated.

### 3.1. Center manifolds

The first tool is one to systematically reduce the dimension of the system further. At the onset of instability, we begin by decomposing the set of differential equations as

$$\dot{x} = Ax + f(x, y), \quad x \in \mathbb{R}^a, \tag{14}$$

$$\dot{y} = By + g(x, y), \quad y \in \mathbb{R}^b. \tag{15}$$

Here, all the eigenvalues of $A$ and $B$ all have zero and negative real parts, respectively. Thus the co-ordinates $x$ represent the critical modes while the $y$ variables are locally stable.

According to the Center Manifold Theorem [19], there exists a $p$-dimensional invariant manifold, $W^c$, lying tangent at $x = y = 0$ to the linear space spanned by the $x$ variables (center eigenspace). Since the critical eigenvalues for the flutter problem occur in a complex conjugate pair, the center eigenspace $E^c$ and the center manifold, $W^c$, are two dimensional ($a = 2$). They are shown schematically in Fig. 5. Invariance implies that solutions starting on $W^c$ remain on the center manifold for all time. Since the vector field of the differential equations contracts in transverse directions, solutions close to the center manifold are attracted to it. Thus local properties such as system stability are determined by the dynamics restricted to the center manifold.

In practice, one often expresses the center manifold $y = h(x)$ explicitly in the form of a power series. Substituting into Eq. (15), we obtain

$$\frac{\partial h}{\partial x}\dot{x} = Bh(x) + g(x, h(x)).$$

Then, employing Eq. (14), invariance is expressed by

$$\frac{\partial h}{\partial x}Ax + \frac{\partial h}{\partial x}f(x, h(x)) = Bh(x) + g(x, h(x)), \tag{16}$$

which can be solved for the coefficients to the power series in $h$. The dynamics on the center manifold which determine the local qualitative behavior of the system thus follow:

$$\dot{x} = Ax + f(x, h(x)). \tag{17}$$

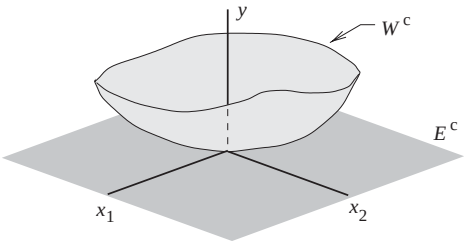


Fig. 5. Schematic representation of the center manifold in the flutter problem.

To study system behavior close to, but not at criticality, one may embed system parameters into the center manifold as discussed in Ref. [20]. Here, the dimension of the center manifold is trivially extended, its dynamics given by

$$\dot{x} = A_\lambda x + f_\lambda(x, h_\lambda(x)), \quad \dot{\lambda} = 0, \tag{18}$$

where $\lambda$ corresponds to one or more system parameters.

### 3.2. Normal forms

The two-dimensional non-trivial center manifold dynamics for flutter are expressed in the form of a power series whose coefficients depend on system parameters and details of the mathematical model. A complementary tool, normal forms, establishes the existence of a co-ordinate transformation, $x = T_\lambda \xi + P_\lambda(\xi)$, that simplifies Eq. (18) considerably. $T_\lambda$ is a matrix crafted to put the linear part of the dynamical system in a canonical form. $P_\lambda(\xi)$ is a vector of polynomials, beginning at quadratic order, whose coefficients are chosen to eliminate certain terms in the ODEs. Application of the Normal Form Theorem [19] tells us that, given a Hopf bifurcation, the equations can be cast into the following simplified form:

$$\begin{aligned} \dot{\xi}_1 &= \xi_1[\sigma_\lambda + c_\lambda(\xi_1^2 + \xi_2^2)] - \xi_2[\omega_\lambda + b_\lambda(\xi_1^2 + \xi_2^2)] + \mathcal{O}(5), \\ \dot{\xi}_2 &= \xi_1[\omega_\lambda + b_\lambda(\xi_1^2 + \xi_2^2)] + \xi_2[\sigma_\lambda + c_\lambda(\xi_1^2 + \xi_2^2)] + \mathcal{O}(5). \end{aligned} \tag{19}$$

Terms of fifth and higher order have been truncated. An initial glance at Eq. (19) may not reveal the utility of normal forms. However, the resulting equations possess rotational symmetry ($SO(2)$) that we may exploit by switching to polar co-ordinates. Defining $r = \sqrt{\xi_1^2 + \xi_2^2}$ and $\vartheta = \tan^{-1}(\xi_2/\xi_1)$, the normal form equations become

$$\dot{r} = \sigma_\lambda r + c_\lambda r^3, \quad \dot{\vartheta} = \omega_\lambda + b_\lambda r^2. \tag{20}$$

The first is an equation for oscillation amplitude which de-couples from $\vartheta$. We note that $\dot{r} \equiv 0$ when $r = 0$ and when $r = \sqrt{-\sigma_\lambda/c_\lambda}$. The point $r = 0$ is a (zero amplitude) equilibrium corresponding to an undisplaced airfoil. Meanwhile, when $\sigma_\lambda$ and $c_\lambda$ are of opposite sign, $r = \sqrt{-\sigma_\lambda/c_\lambda}$ corresponds to a finite amplitude limit cycle. In Fig. 6(a), we depict typical behaviors for different values of $\sigma_\lambda$ and $c_\lambda$.

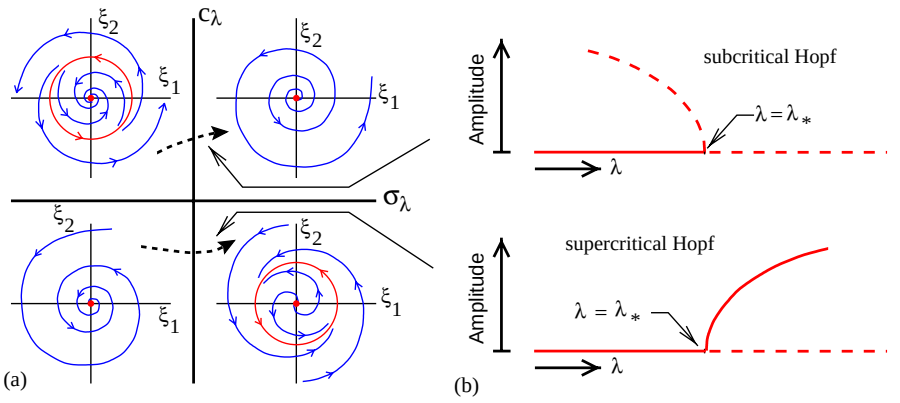


Fig. 6. (a) Typical phase portraits for different values of $\sigma_\lambda$ and $c_\lambda$. (b) The two generic types of Hopf bifurcation.

As we vary a system parameter $\lambda$ (e.g., flow speed), the values of $\sigma_\lambda$ and $c_\lambda$ change. We let $\lambda_*$ denote the critical value at which instability occurs (i.e., $\sigma_{\lambda_*} = 0$), and without loss of generality, we assume $\sigma_\lambda < 0$ (resp. $\sigma_\lambda > 0$) for $\lambda < \lambda_*$ (resp. $\lambda > \lambda_*$). Generically we expect $c_{\lambda_*} \neq 0$. Therefore, as we continuously vary $\lambda$ in a neighborhood of $\lambda_*$, we trace out a curve in the $\sigma_\lambda$, $c_\lambda$ plane similar to one of the dashed curves in Fig. 6(a). If $c_{\lambda_*} > 0$, we say that the Hopf bifurcation is subcritical. For $c_{\lambda_*} < 0$, it is supercritical. Qualitative sketches in amplitude $\times$ parameter space depicting the emergence of periodic orbits are given in Fig. 6(b). Note that at $\lambda = \lambda_*$, the zero amplitude equilibrium changes stability: the solid line (stable) becomes dashed (unstable). Arrows indicate regions in which oscillation amplitudes either grow or decay. In the supercritical case, the instability spawns a stable periodic solution for $\lambda > \lambda_*$, whose amplitude grows like $k\sqrt{\lambda - \lambda_*}$ initially. In the subcritical case, the periodic orbit is unstable and lies on the stable side of the bifurcation. This latter case is recognized to be potentially dangerous: because of the unstable limit cycle in the vicinity of the origin, small but finite perturbations may lead to growing oscillations even though the system is linearly stable.

To determine whether a flutter instability is subcritical or supercritical, it is merely necessary to check the sign of $c_{\lambda_*}$. At $\lambda = \lambda_*$, the first of Eq. (18) becomes

$$\dot{x}_1 = \omega_{\lambda_*} x_2 + f_1(x_1, x_2), \quad \dot{x}_2 = -\omega_{\lambda_*} x_1 + f_2(x_1, x_2).$$

Guckenheimer and Holmes [19] report that the cubic normal form coefficient can be calculated by

$$c_{\lambda_*} = \tfrac{1}{16}(f_{1,111} + f_{1,122} + f_{2,112} + f_{2,222}) + \frac{1}{16\omega_{\lambda_*}}[f_{1,12}(f_{1,11} + f_{1,22}) - f_{2,12}(f_{2,11} + f_{2,22}) - f_{1,11}f_{2,11} + f_{1,22}f_{2,22}], \tag{21}$$

where subscripts after the comma denote partial derivatives, i.e.,

$$f_{j,\ell mn} := \left.\frac{\partial^3 f_j}{\partial x_\ell \partial x_m \partial x_n}\right|_{x=0}.$$

Thus, to determine of the criticality of the Hopf bifurcation, we need only to perform a small algebraic calculation rather than the full normal form transformation—usually a messy task. This

approach lies in stark contrast to efforts previously referenced in which sub- or supercriticality was determined by painstaking numerical integration. Even numerical continuation packages such as AUTO [21] or CONTENT [22] require direct numerical simulation to follow branches of periodic orbits. The center manifold/normal form approach affords us the opportunity to easily perform a more thorough parametric study of the classical flutter problem with structural non-linearities, and hence test conjectures of previous authors.

Although we apply the normal form approach to a relatively simple Theodorsen-like model, there is no inherent limitation that would prevent it from being applied to more sophisticated models incorporating three-dimensional or transonic flow, structural damping, or other effects, provided suitable models can be derived. Implicit in the normal form approach, though, is that the structural non-linearities of the system are well approximated by Taylor series truncated at cubic order. This means that the normal form approach might not be applicable to systems with some common non-smooth non-linearities such as free-play. A somewhat encouraging exploration of this subject, in a different context, is presented in Ref. [23].

We begin our exploration with cubic structural non-linearities and then elaborate on effects of quadratic non-linearities.

## 4. Cubic structural non-linearities

We begin by considering cases for which the only non-linearity of the system appears as cubic restoring forces in the springs: $\delta_{\alpha 2} = \delta_{h2} = 0$; $\delta_{\alpha 3} \neq 0$, and/or $\delta_{h3} \neq 0$. These cases provide an immediate means of comparison with results from previous authors, and they are easiest to calculate.

Their simplicity derives from the fact that the center manifold becomes irrelevant in the cubic order analyses. To illustrate, we observe that in Eq. (18), $f_\lambda(x,y) = f_\lambda^{(3)}(x,y) + f_\lambda^{(4)}(x,y) + \mathcal{O}(5)$, where $f_\lambda^{(3)}$ and $f_\lambda^{(4)}$ contain cubic and quartic order terms, respectively. Since the center manifold is tangent to the center eigenspace, the lowest order terms in its Taylor series expansion are quadratic. Hence, the center manifold may be written as $y = h_\lambda(x) = h_\lambda^{(2)}(x) + h_\lambda^{(3)}(x) + \mathcal{O}(4)$. Upon substitution into Eq. (18), the cubic order equations on the center manifold become

$$\dot{x} = A_\lambda x + f_\lambda^{(3)}(x,0) + \mathcal{O}(4). \tag{22}$$

Thus, when determining the criticality of the Hopf bifurcation via the cubic order normal form coefficient in Eq. (21), one does not need to compute the center manifold. Further, all the second derivatives on the second line of Eq. (21) vanish. Since Eq. (21) is a linear combination of third derivatives of $f_{\lambda_*}^{(3)}$, it is simple to verify that the normal form coefficient takes the form

$$c_{\lambda_*} = p\delta_{\alpha_3} + q\delta_{h_3}, \tag{23}$$

where the constants $p$ and $q$ depend on other system parameters.

Within the $\delta_{\alpha_3}$, $\delta_{h_3}$ parameter space, the line $p\delta_{\alpha_3} + q\delta_{h_3} = 0$ shown in Fig. 7 separates subcritical from supercritical Hopf bifurcations. The relative values of the coefficients $p$ and $q$ determine the orientation $\theta \in [-\pi, \pi)$ of this boundary. When $\theta > 0$, as shown in the figure, the flutter criticality hypothesis holds: a hard pitch spring produces a supercritical bifurcation while a

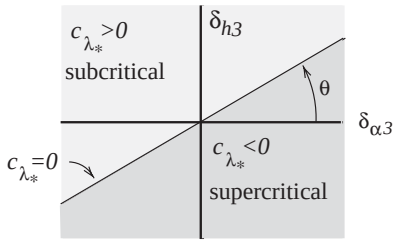


Fig. 7. A boundary line that separates supercritical from subcritical Hopf bifurcations in $\delta_{\alpha 3}$, $\delta_{h3}$ parameter space.

soft spring yields a subcritical instability. Cases for which $\theta<0$ represent counterexamples to the hypothesis.

### 4.1. Typical results

In Figs. 8(a) and (b), we hold the parameters $\mu$, $\xi_{ea}$, and $r_\alpha$ fixed. The first shows level curves of the flutter speed $\tilde{U}_F$ as the parameters $X$ and $\chi$ vary. The largest level set shown coincides with the divergent flutter speed $\tilde{U}_D = \sqrt{\mu r_\alpha^2/(2\xi_{ea}-1)}$ [24], beyond which the aeroelastic instability is not of the oscillatory Hopf type; a purely real eigenvalue crosses the imaginary axis.

For the same set of parameter values, we show in Fig. 8(b) level sets for $\theta$, the orientation of the criticality boundary. Since the normal form approach allows us to determine criticality of more a thousand cases in roughly a second of time using a common desk-top computer, generating data for the figure is quite feasible. For reference, the level sets of $\tilde{U}_F$ are overlaid as dotted curves in Fig. 8(b). The shaded region indicates parameter regions for which $\theta<0$. For these parameters, the flutter criticality hypothesis does not hold.

Three slices at $\chi = 0.1$, 0.2, and 0.3 through the data of Fig. 8 are shown in Figs. 9(a), (b), and (c), respectively. Both $\theta$ and $\tilde{U}_F$ are depicted. For $\chi = 0.1$, the angle $\theta$ jumps by $-\pi$ as the flutter boundary touches $\tilde{U}_F = 0$. Thus, the regions of the $\delta_{\alpha_3}\delta_{h_3}$ parameter space (Fig. 7) in which sub- and supercritical Hopf bifurcations occur are suddenly interchanged. We provide a physical explanation in Section 4.4. For $\chi = 0.2$ and 0.3, flutter boundaries are safely separated from zero, and $\theta$ varies continuously with respect to $X$, although changes may be abrupt. In Section 4.4, we provide a physical explanation for the sudden jumps. Before doing so, though, we demonstrate numerically that the normal form analysis predicts correct dynamic behavior.

### 4.2. Numerical agreement: model equations

We begin our numerical comparison and verification with the model equations (1) with fourth order aerodynamics as described in Section 2.2. Typical parameters we use for an illustrative example are: $\mu = 20$, $\xi_{ea} = 0.6$, $r_\alpha = 0.5$, $\chi = 0.1$, and $X = 1.7$. The flutter corresponding speed is $\tilde{U}_F = 3.778$. According to theoretical predictions in Figs. 8 and 9(a), this is a case which contradicts the flutter criticality hypothesis.

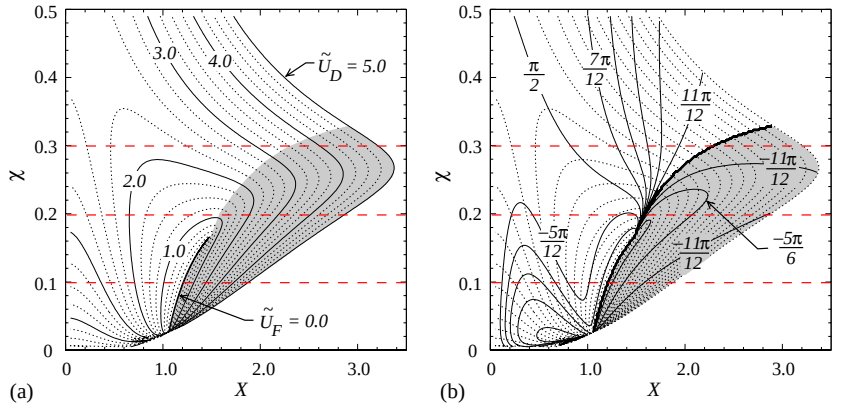


Fig. 8. (a) Level curves depicting parameters $X$ and $\chi$ for which $\tilde{U}_F = const$. (b) Level curves of $\theta$ with level curves of $\tilde{U}_F$ shown dotted. In all calculations, $\mu = 20$, $\xi_{ea} = 0.6$, and $r_\alpha = 0.5$. In shaded regions, we find counterexamples to the flutter criticality hypothesis. Dashed lines represent slices of parameter space depicted in Fig. 9.

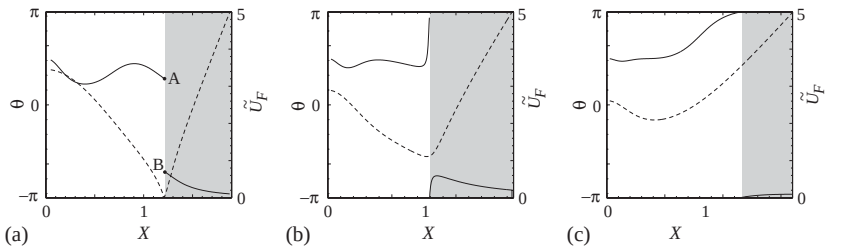


Fig. 9. Plots of the orientation $\theta$ (solid) and flutter velocity $\tilde{U}_F$ (dashed) for three slices of parameter spaced, shown dashed, in Fig. 8: (a) $\chi = 0.1$; (b) $\chi = 0.2$; (c) $\chi = 0.3$. Other parameters held fixed are $\mu = 20$, $\xi_{ea} = 0.6$, and $r_\alpha = 0.5$. In shaded regions, we find counterexamples to the flutter criticality hypothesis.

First we observe that when $\tilde{U} = 0$, the system is Hamiltonian with conserved energy

$$E = \frac{1}{2}\left(1 + \frac{1}{\mu}\right)\tilde{h}'^2 - \left(\chi - \frac{1}{\mu}(\xi_{ea} - 1)\right)\tilde{h}'\alpha' + \frac{1}{2}\left(r_\alpha^2 + \frac{1}{\mu}(\xi_{ea} - 1)^2 + \frac{1}{8\mu}\right)\alpha'^2 + r_\alpha^2\tilde{V}. \tag{24}$$

When $\tilde{U} \neq 0$, the Hamiltonian structure is destroyed, but $E$ provides a good scalar measure of the oscillation amplitude. Several plots of this amplitude measure are shown in Figs. 10(b) and (c) versus dimensionless time, $\tau$. Despite the hard spring ($\delta_{\alpha_3} = 50$) used in first set of simulations, Fig. 10 clearly shows subcritical behavior. Sufficiently small perturbations decay as expected, since the flow speed is set below the flutter velocity ($\tilde{U} = 0.9\tilde{U}_F$). Slightly larger initial conditions grow due the presence of an unstable limit cycle. The example contradicts the flutter criticality hypothesis, but agrees with our normal form analysis.

When the spring is soft ($\delta_{\alpha_3} = -10$) in Fig. 10(c), with flow speed set slightly above flutter velocity ($\tilde{U} = 1.1\tilde{U}_F$), initial conditions are attracted to a stable periodic orbit. This indicated the

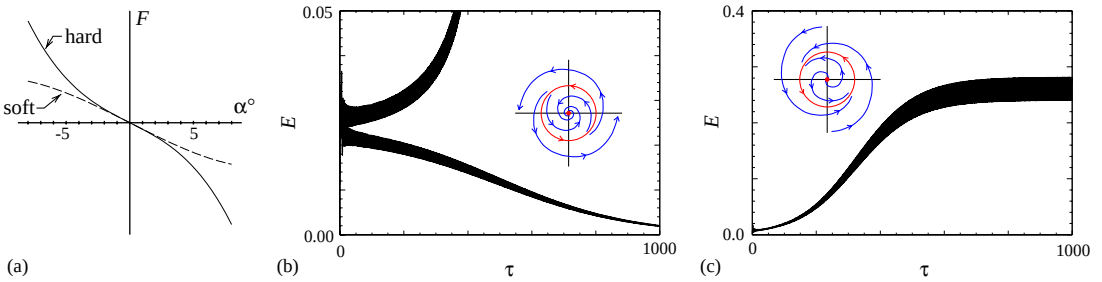


Fig. 10. Simulations of the eighth order model of Section 2.1 illustrating a contradiction to the flutter criticality hypothesis. System parameters are listed in the text. The only structural non-linearities are cubic non-linearities in the pitch spring (a). For simulations in (b), the pitch spring is hard: $\delta_{\alpha_3} = 50$, and flow velocity is below critical: $\tilde{U} = 0.9\tilde{U}_F$. For simulations in (c) $\delta_{\alpha_3} = -10$, and $\tilde{U} = 1.1\tilde{U}_F$. Qualitative phase portraits indicating subcritical and supercritical behavior, respectively, are also depicted.

presence of a supercritical Hopf bifurcation, again contradicting the flutter hypothesis, yet agreeing with our analysis.

As demonstrated by Liu et al. [15], the amplitudes of limit cycles are well approximated by $r = \sqrt{-\sigma_\lambda/c_\lambda}$, modulo the scalings embedded in the normal form transformations. In both sets of solutions, the effective angles of incidence on the airfoil remain well below 10°, supporting our modelling assumption of attached flow.

### 4.3. Numerical agreement: high fidelity simulation

To demonstrate that this contradictory behavior is not an artifact of modelling approximations employed in Section 2.1. We perform a second set of simulations of a high fidelity model similar to those of Kim and Mook [25] and Hall [26]. Here, the airfoil is treated as a flat plate on which we distribute bound vorticity in the form of Glauert modes [27]:

$$\tilde{\gamma}(\xi,\tau) = 2\tilde{U}\left[A_0(\tau)\frac{1+\cos(\phi)}{\sin(\phi)} + \sum_{n=1}^{\infty} A_n(\tau)\sin(n\phi)\right], \tag{25}$$

which automatically satisfies the Kutta condition, and where $\phi$ and $\xi$ are related by $\xi = (1-\cos(\phi))$. The time dependent modal coefficients $A_n(t)$ are chosen to satisfy non-penetration conditions, cancelling the upwash, $W(x,t) = W^{(m)}(\xi,\tau) + W^{(w)}(\xi,\tau)$, induced by blade motion ($W^{(m)}$) and vorticity in the wake ($W^{(w)}$). As illustrated schematically in Fig. 11, the wake is represented by a flat line of point vortices, one shed at each time step to satisfy Kelvin's circulation theorem. The vortices are then convected downstream by the mean flow. Lifts and moments can be calculated by

$$\begin{aligned}\tilde{L} &= \frac{1}{\pi\tilde{U}}\int_0^2 \tilde{\gamma}(\xi)\,\mathrm{d}\xi + \frac{1}{\pi\tilde{U}^2}\int_0^2\int_0^{\xi}\tilde{\gamma}(\hat{\xi})'\,\mathrm{d}\hat{\xi}\,\mathrm{d}\xi,\\ \tilde{M}_{ea} &= \frac{1}{\pi\tilde{U}}\int_0^2 (\xi_{ea}-\xi)\tilde{\gamma}(\xi)\,\mathrm{d}\xi + \frac{1}{\pi\tilde{U}^2}\int_0^2 (\xi_{ea}-\xi)\int_0^{\xi}\tilde{\gamma}(\hat{\xi})'\,\mathrm{d}\hat{\xi}\,\mathrm{d}\xi.\end{aligned} \tag{26}$$

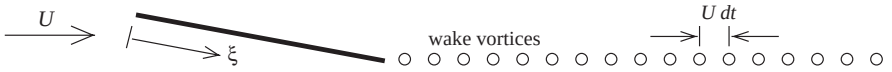


Fig. 11. Schematic of high fidelity simulation.

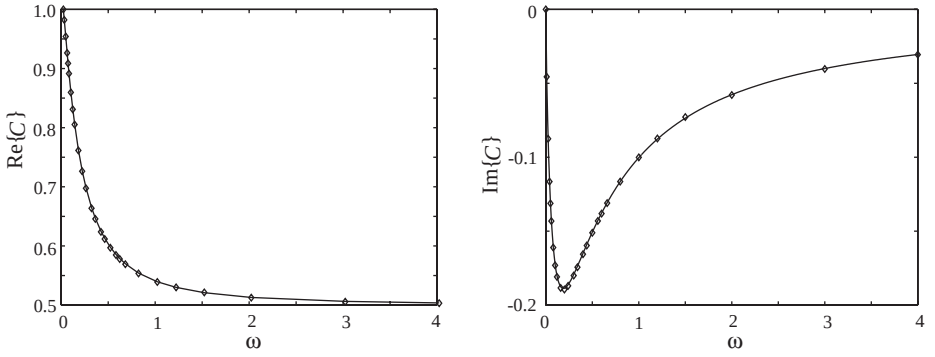


Fig. 12. Comparison of Theodorsen's function (solid) to the frequency response of the high fidelity simulation (symbols).

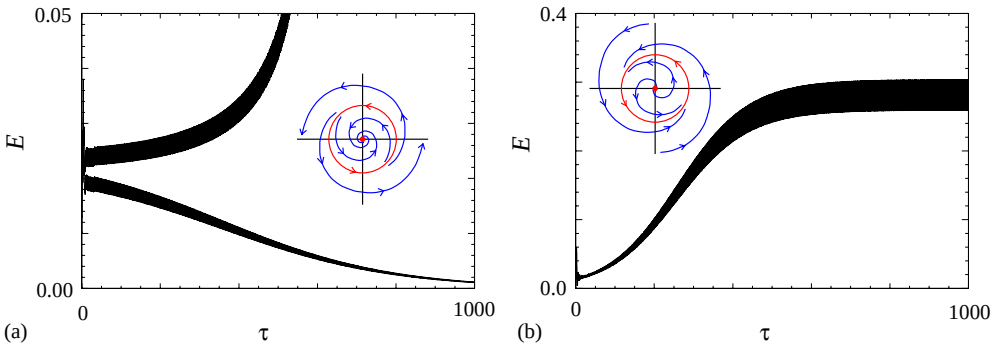


Fig. 13. High fidelity simulations confirming the presence of contradictions to the flutter criticality hypothesis. Parameters and initial conditions in (a) and (b) are identical to those of Figs. 10(b) and (c), respectively.

Once the aerodynamic forces, involving the Glauert modes and hundreds of point vortices, are incorporated into the equations of motion (1), the dynamical system may be integrated numerically. In Fig. 12, we compare the in-phase and out-of-phase components of the frequency response of the high fidelity simulation to the real and imaginary parts of Theodorsen's function. Once we subtract off apparent mass effects, the numerical simulations (symbols) agree very well with the theoretical curves.

Finally, in Fig. 13, we plot results from the high fidelity numerical simulations with parameters and initial conditions chosen to be completely analogous to those of the eighth order model presented in Fig. 10. Again, we observe the hard-subcritical/soft-supercritical bifurcation which contradicts the flutter criticality hypothesis. It is almost identical to the low order model, and exactly as predicted by the theory.

### 4.4. Physical insight

As we saw in Fig. 8, the angle $\theta$ of the boundary in $(\delta_{\alpha_3}, \delta_{h_3})$ space that separates subcritical from supercritical systems, can change rapidly (even discontinuously) as parameters are changed smoothly. Furthermore, this rapid change appears to coincide with the boundary between systems which do and do not satisfy the flutter hypothesis. To provide a physical explanation, we turn to the situation for $\chi = 0.1$ of Fig. 9(a) in which the change is most dramatic. Specifically we consider $X = X_A = 1.21$ and $X = X_B = 1.212113$ which we shall refer to as systems A and B, respectively. They are labelled in Fig. 9(a). Although the parameters for the two systems are nearly identical, the former obeys the flutter criticality hypothesis with $\theta = 0.89$ rad while the latter contradicts the hypothesis with $\theta = -2.25$ rad. In both systems $\tilde{U}_F \approx 0.0082$. At the onset of instability, $\tilde{U} = \tilde{U}_F$, the linearized ($\delta_{h_2} = \delta_{h_3} = \delta_{\alpha_2} = \delta_{\alpha_3} = 0$) equations of motion possess a sinusoidal solution of the form $\alpha = \cos(\omega\tau)$, $h = H\cos(\omega\tau + \phi)$, where $H$, $\omega$, and $\phi$ are determined from eigenvectors and eigenvalues. Since the critical eigens vary continuously in this parameter neighborhood, the sinusoidal solutions to the linearized systems corresponding to systems A and B are nearly identical.

To illuminate the dramatic differences in non-linear behavior between the two nearly identical systems, we look at the mechanical work generated by the fluid on the motion of the blade. Of the numerous terms in lift (3), only the terms $\tilde{L}_{1/4} = 2\tilde{G}$ and $\tilde{L}_{3/4} = \alpha'/\tilde{U}$ are capable of producing net work per period of the sinusoidal oscillation. The remaining terms have a Hamiltonian structure and thus preserve energy measures. The subscripts of the lift components refer to the centers of pressure at which they act: $\frac{1}{4}$- and $\frac{3}{4}$-chord, respectively. Work per cycle, therefore, is $\mathbb{W} = \mathbb{W}_{1/4} + \mathbb{W}_{3/4}$, where

$$\mathbb{W}_{1/4} = \int_{\tau_0}^{\tau_0+T} \tilde{L}_{1/4}(\tau)\tilde{v}_{1/4}(\tau)\,\mathrm{d}\tau, \quad \mathbb{W}_{3/4} = \int_{\tau_0}^{\tau_0+T} \tilde{L}_{3/4}(\tau)\tilde{v}_{3/4}(\tau)\,\mathrm{d}\tau. \tag{27}$$

Here, $\tilde{v}_{1/4}$ and $\tilde{v}_{3/4}$ are the vertical components of the airfoil velocity at their respective locations on the chord.

In Fig. 14(a), we plot time traces of the two components of power, $\tilde{P}_j = \tilde{L}_j\tilde{v}_j$. One period of oscillation is presented. In system A, $\tilde{P}_{1/4}$ is mostly positive, while $\tilde{P}_{3/4}$ is mostly negative. Therefore, the two contributions, $\mathbb{W}_{1/4}$ and $\mathbb{W}_{3/4}$, to the total work per cycle will be positive and negative, respectively. Since the plots were computed at the critical flow speed, the net work must be zero: $\mathbb{W}_{1/4} + \mathbb{W}_{3/4} = 0$. We present an analogous plot of the powers over one period of the

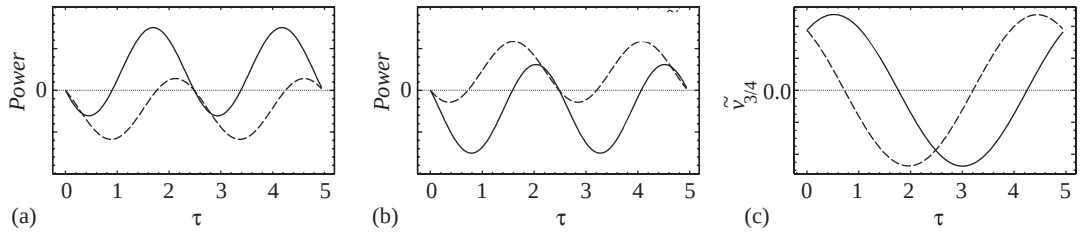


Fig. 14. (a,b) Non-trivial components of power induced by aerodynamic forces on airfoil. In both subfigures, the solid curves correspond to $\tilde{P}_{1/4}$ while dashed curves correspond to $\tilde{P}_{3/4}$. Subfigure (a) corresponds to Case A from Fig. 9, and (b) corresponds to Case B. (c) Vertical component of blade velocity at $\frac{3}{4}$ chord point: Case A (solid); Case B (dashed).

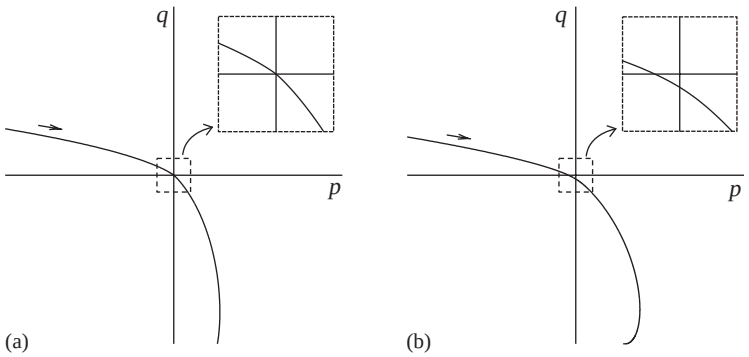


Fig. 15. (a) Migration of the $p$ and $q$ coefficients in Eq. (23) in a case with zero velocity flutter, $\chi = 0.1$. (b) A case without zero velocity flutter, $\chi = 0.2$.

sinusoidal solution of system B in Fig. 14(b). Again, $\mathbb{W}_{1/4} + \mathbb{W}_{3/4} = 0$. However, the roles of $\tilde{P}_{1/4}$ and $\tilde{P}_{3/4}$ have suddenly and completely reversed: $\tilde{P}_{1/4}$ produces net negative work while $\tilde{P}_{3/4}$ generates positive work.

Between systems A and B, $\tilde{L}_{3/4}$ and $v_{1/4}$ vary only imperceptibly. The velocity at the $\frac{3}{4}$-chord location, though, undergoes an abrupt phase shift as shown in Fig. 14(c). Furthermore, since $\tilde{L}_{1/4}$ depends directly on the upwash at the $\frac{3}{4}$-chord location, it experiences the same shift and hence both components of the work shift accordingly.

The abrupt phase shift is symptomatic of zero flow velocity flutter ($\tilde{U}_F = 0$), a phenomenon first illuminated by Biot and Arnold [28]. The flutter velocity falling to zero as parameters vary coincides with a nodal point of one of the vibration modes passing through the $\frac{3}{4}$-chord location. In other words, pitch and plunge are co-ordinated so that the airfoil rotates about its $\frac{3}{4}$-chord point, which remains motionless. When varying $X$ from system A to system B, the fact that $v_{3/4}$ passes through zero causes the abrupt change in the phase of the normalized velocity $\tilde{v}_{3/4}$.

When we include structural non-linearities, the solutions get distorted somewhat, and the two components of work generally will not balance at $\tilde{U} = \tilde{U}_F$. If the negative component of work is enhanced relative to the positive, the system non-linearities provide a stabilizing effect indicative of a supercritical Hopf bifurcation. Similarly, a net positive work by the non-linear terms signifies a subcritical instability. The fact that the negative components of work suddenly become positive components of work and vice versa between systems A and B causes the sudden change in the nature of the flutter criticality.

In Fig. 15(a), we plot the coefficients $p$ and $q$ of Eq. (23) as $X$ varies in the neighborhood of systems A and B. At zero flutter, $\tilde{U} = \tilde{U}_F = 0$, the system is Hamiltonian and hence energy is conserved. At this instant, $c_{\lambda_*}$ is identically zero and hence $p \equiv q \equiv 0$. Therefore the curve in Fig. 15(a) must pass through the origin, explaining the jump by $\pi$ in the quantity $\theta = \tan^{-1}(p/q)$.

When $\tilde{U} = \tilde{U}_F = 0$, energy (24) is conserved and hence the normal form coefficient $c_{\lambda_*}$ in Eq. (20) is identically zero: ($p = q = 0$). This explains the jump in $\theta$ by $\pi$ in Fig. 9(a). For situations such as those shown in Figs. 9(b) and (c), there is no zero velocity flutter and hence no discontinuous jump in $\theta$. However, the center of rotation, although not on the blade, does pass

close to the $\frac{3}{4}$-chord location, causing the $(p, q)$ curve in Fig. 15(b) to pass close to the origin and hence cause an abrupt change in $\theta$.

### 4.5. Counterexamples to flutter hypothesis prevail

Although we state that the results of Section 4.1 are typical, we have not demonstrated this. In particular, one may be interested in the degree to which counterexamples to the flutter criticality hypothesis prevail. Therefore, consider Figs. 16–19 in which we show level sets of $\tilde{U}_F$ and $\theta$, analogous to Figs. 8(a) and (b).

In Figs. 16 and 18, the dimensionless radius of gyration, $r_\alpha$, about the elastic axis takes the values 0.5, 0.8, 1.2, while the chosen values of elastic axis location, $\xi_{ea}$, are 0.2, 0.6, 1.0, 1.4, 1.8. The mass ratio is constant at $\mu = 20$. In the plots of Figs. 17 and 19, we fix $r_\alpha = 0.5$, allow $\xi_{ea}$ to vary as before, and choose $\mu = 10$, 40, 80. Within the individual plots, bounds on $X$ and $\chi$ are typically chosen to cover all possible values for which the oscillatory flutter occurs. However, since divergent flutter does not occur for $\xi_{ea} < 0.5$, we show only level sets for $\tilde{U}_F \leqslant 10.0$ in these cases. As in Fig. 8, we shade regions which contradict the flutter criticality hypothesis.

Although the details differ, the plots exhibit common features. All show regions which contradict the flutter criticality hypothesis, some more prominently than others. In all, there is a curve in parameter space corresponding to zero flow speed flutter, $U_F = 0$. The criticality boundary angle, $\theta$, jumps discontinuously by $\pi$ across the zero flutter curves, similar to that depicted in Fig. 9(a). On those parts of the boundaries between shaded and unshaded Hopf regions which do not coincide with $\tilde{U}_F = 0$, the angle $\theta$ varies continuously from $-\pi$ to $\pi$. Thus the case we studied in detail in previous subsections is representative of flutter phenomena in general.

One may notice that the plots with $\xi_{ea} = 0.2$ differ from the others: they do not exhibit divergent flutter, and there are two distinct boundaries which separate Hopf bifurcations which do and do not obey the flutter criticality hypothesis. In Fig. 20(a), we show level sets of $\theta$ for such a system with $\xi_{ea} = 0.2$, $\mu = 20$, $r_\alpha = 0.5$. Figs. 20(b) and (c) show data for $\tilde{U}_F$ and $\theta$ along slices of the parameter space at $X = 0.75$ and 2.0, respectively. The first is rather uneventful, however, the second slice passes through both boundaries of the shaded region. On the first boundary crossing near $\chi = 0.08$, $\theta$ varies continuously from $\pi$ to $-\pi$. The second boundary crossing near $\chi = 0.138$ is one for which the system passes through zero speed flutter and $\theta$ jumps by $\pi$.

## 5. Quadratic non-linearities

When we include quadratic non-linearities in the restoring forces, we break the reflection symmetry, $(h, \alpha) \mapsto (-h, -\alpha)$, of the system. Nonetheless, the physical problem still possesses a higher order symmetry: the equations of motion are equivariant under the transformation $(h, \alpha, \delta_{h_2}, \delta_{\alpha_2}) \mapsto (-h, -\alpha, -\delta_{h_2}, -\delta_{\alpha_2})$. Therefore, the cubic normal form coefficient $c_{\lambda_*}$ of Eq. (21) must be invariant under $(\delta_{h2}, \delta_{\alpha 2}) \mapsto (-\delta_{h2}, -\delta_{\alpha 2})$. This means that, regardless of which direction the symmetry is broken, the qualitative nature of the instability is the same.

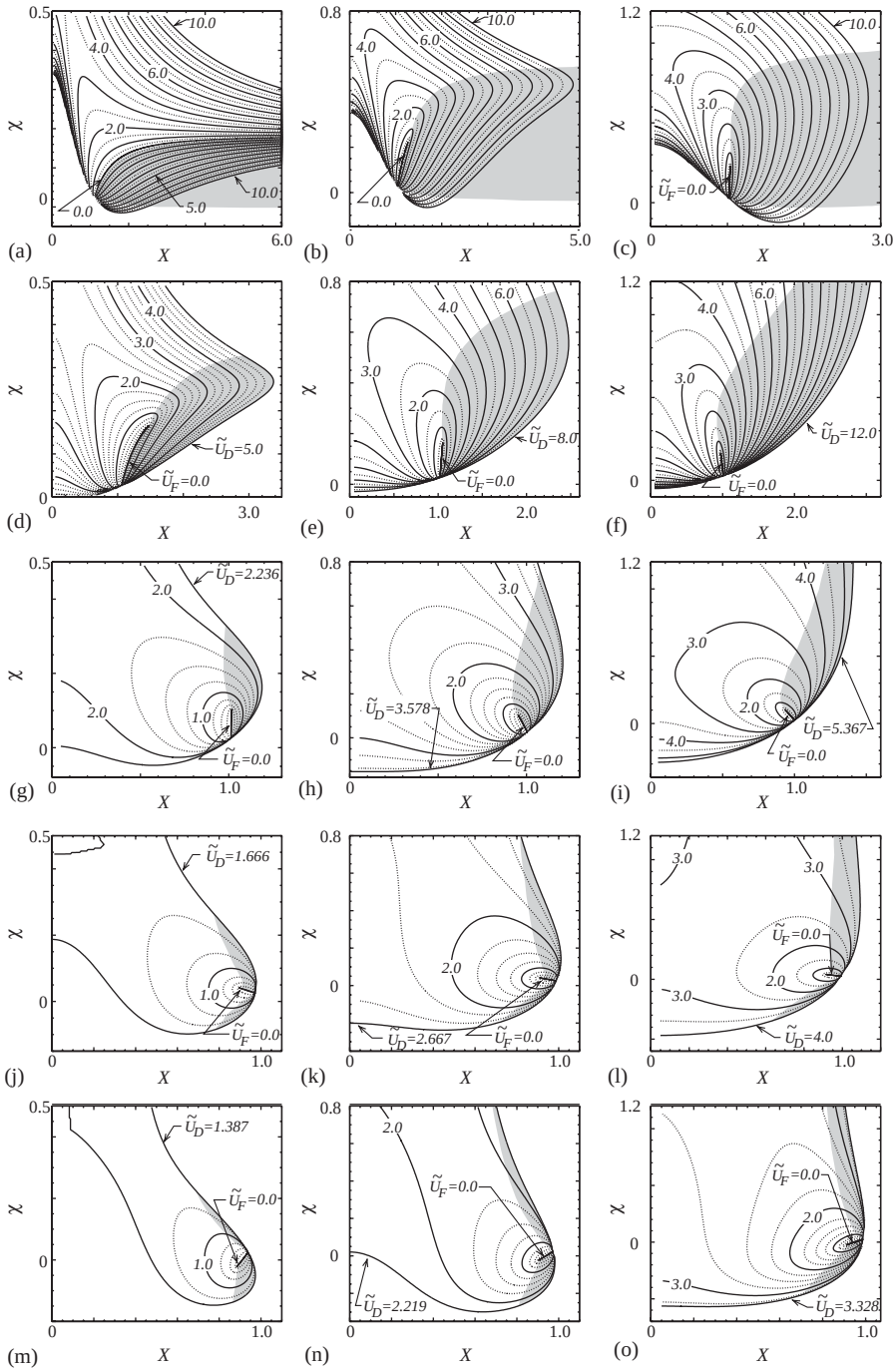


Fig. 16. Level curves of $\tilde{U}_F$, holding mass ratio fixed at $\mu = 20$. (a) $\xi_{ea} = 0.2$, $r_\alpha = 0.5$; (b) $\xi_{ea} = 0.2$, $r_\alpha = 0.8$; (c) $\xi_{ea} = 0.2$, $r_\alpha = 1.2$; (d) $\xi_{ea} = 0.6$, $r_\alpha = 0.5$; (e) $\xi_{ea} = 0.6$, $r_\alpha = 0.8$; (f) $\xi_{ea} = 0.6$, $r_\alpha = 1.2$; (g) $\xi_{ea} = 1.0$, $r_\alpha = 0.5$; (h) $\xi_{ea} = 1.0$, $r_\alpha = 0.8$; (i) $\xi_{ea} = 1.0$, $r_\alpha = 1.2$; (j) $\xi_{ea} = 1.4$, $r_\alpha = 0.5$; (k) $\xi_{ea} = 1.4$, $r_\alpha = 0.8$; (l) $\xi_{ea} = 1.4$, $r_\alpha = 1.2$; (m) $\xi_{ea} = 1.8$, $r_\alpha = 0.5$; (n) $\xi_{ea} = 1.8$, $r_\alpha = 0.8$; (o) $\xi_{ea} = 1.8$, $r_\alpha = 1.2$.

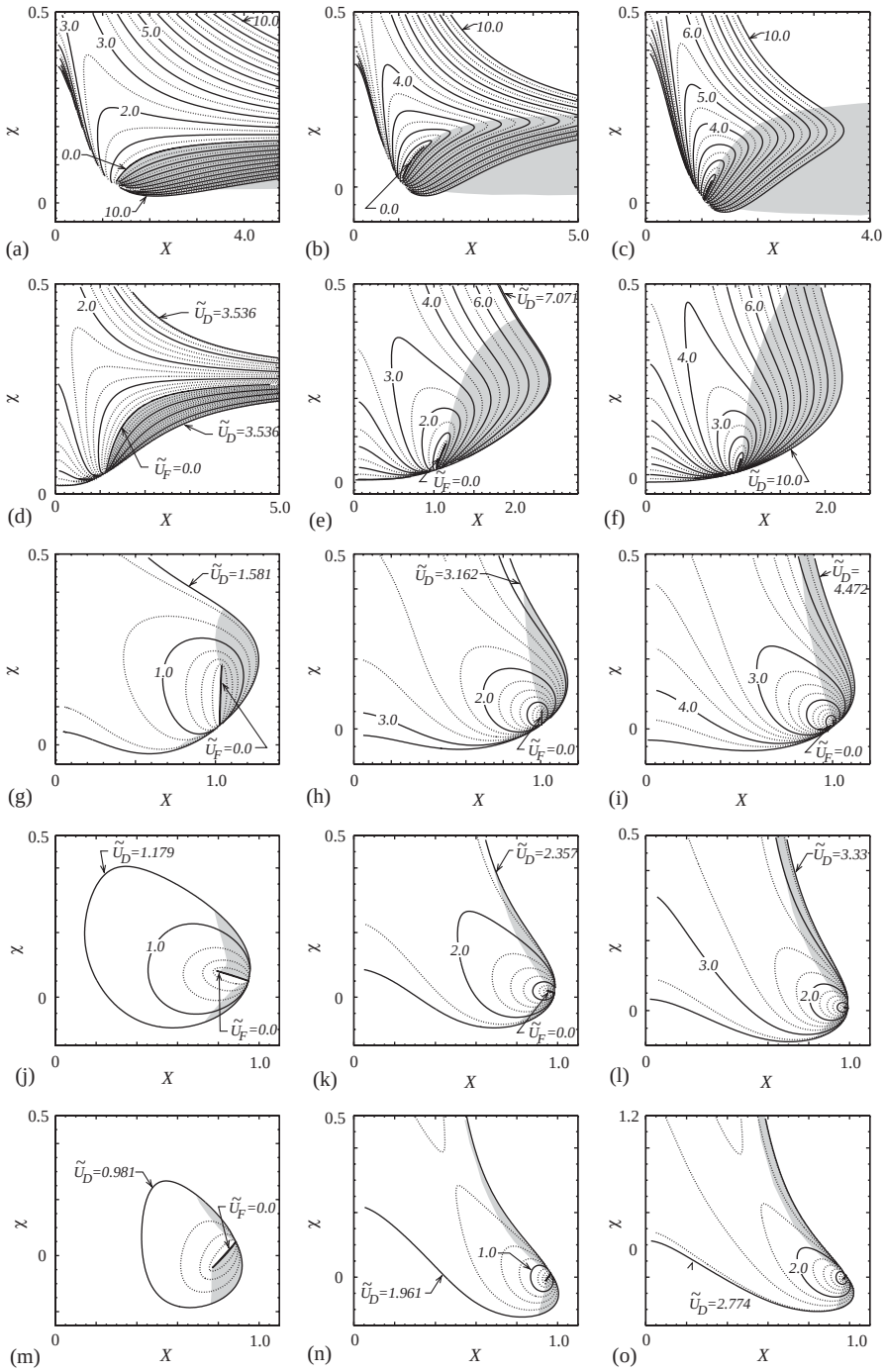


Fig. 17. Level curves of $\tilde{U}_F$, holding radius of gyration fixed at $r_\alpha = 0.5$. (a) $\xi_{ea} = 0.2$, $\mu = 10$; (b) $\xi_{ea} = 0.2$, $\mu = 40$; (c) $\xi_{ea} = 0.2$, $\mu = 80$; (d) $\xi_{ea} = 0.6$, $\mu = 10$; (e) $\xi_{ea} = 0.6$, $\mu = 40$; (f) $\xi_{ea} = 0.6$, $\mu = 80$; (g) $\xi_{ea} = 1.0$, $\mu = 10$; (h) $\xi_{ea} = 1.0$, $\mu = 40$; (i) $\xi_{ea} = 1.0$, $\mu = 80$; (j) $\xi_{ea} = 1.4$, $\mu = 10$; (k) $\xi_{ea} = 1.4$, $\mu = 40$; (l) $\xi_{ea} = 1.4$, $\mu = 80$; (m) $\xi_{ea} = 1.8$, $\mu = 10$; (n) $\xi_{ea} = 1.8$, $\mu = 40$; (o) $\xi_{ea} = 1.8$, $\mu = 80$.

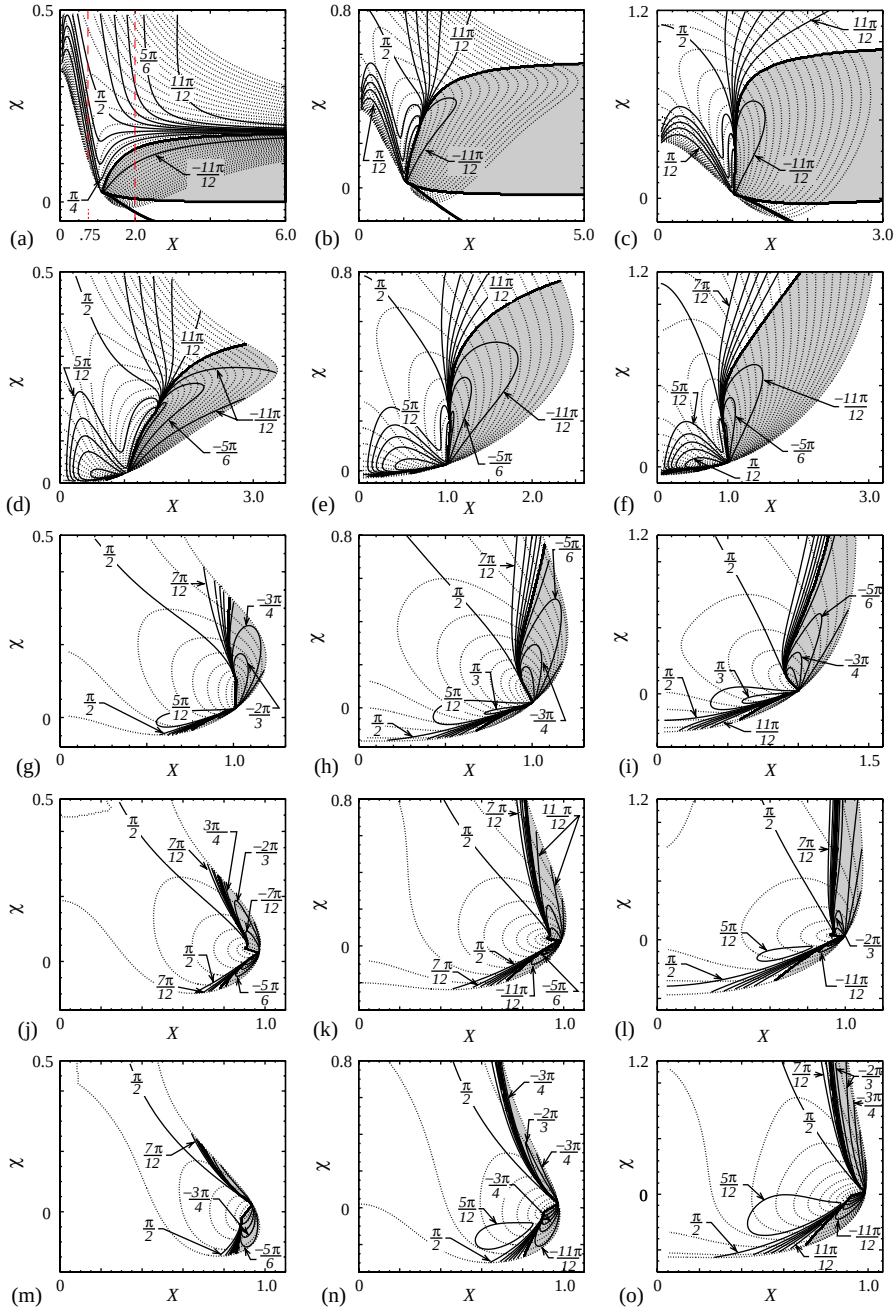


Fig. 18. Level curves of $\theta$, juxtaposed with level curves of $\tilde{U}_F$. Parameters are the same as those in Fig. 16.

To formally account for the quadratic non-linearities in the calculation of $c_{\lambda_*}$, it becomes necessary to incorporate the center manifold into the analysis. If we let $g^{(2)}(x, y)$ denote the quadratic part of $g(x, y)$ in Eq. (15), then the quadratic part of $g(x, h(x))$ in Eq. (16) is $g^{(2)}(x, 0)$.

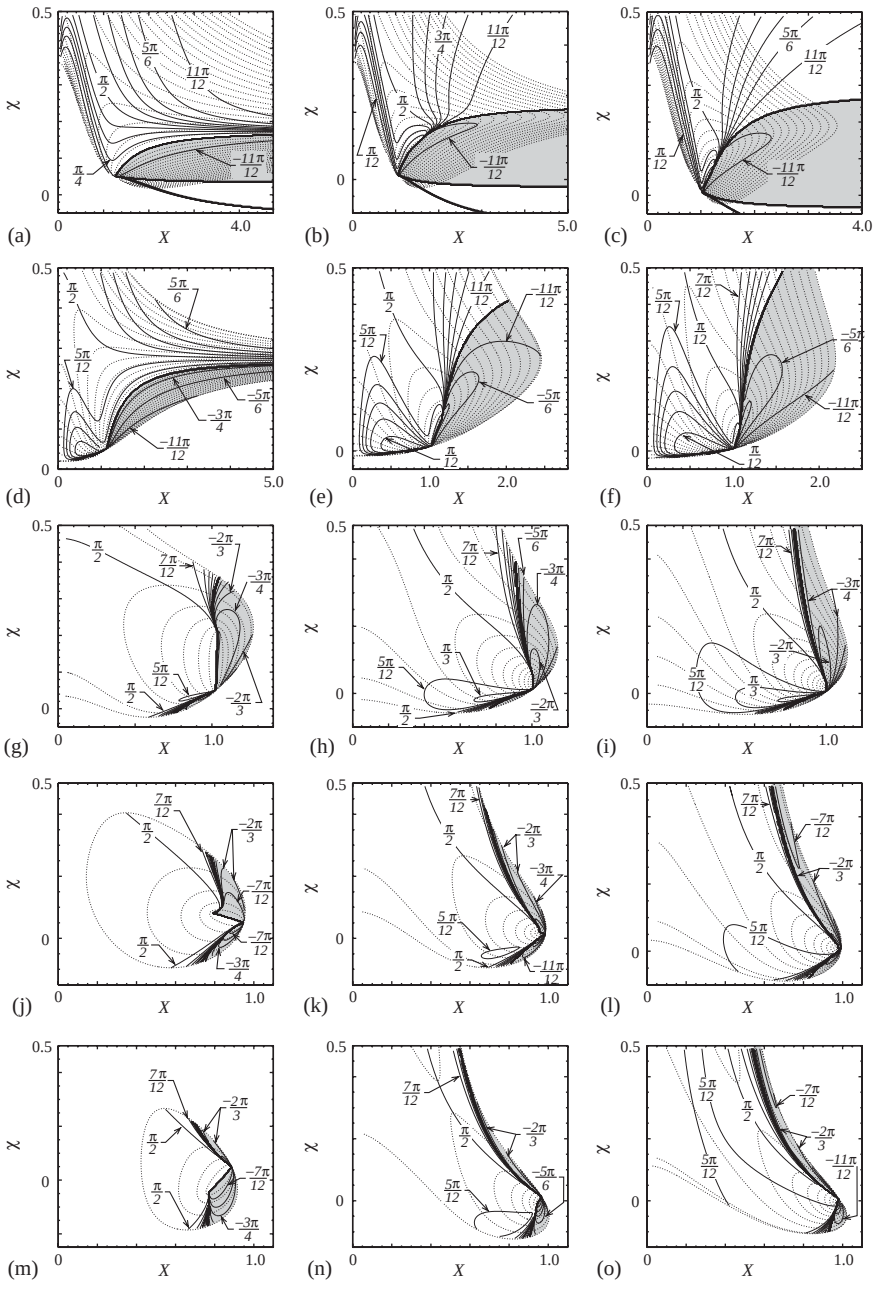


Fig. 19. Level curves of $\theta$, juxtaposed with level curves of $\tilde{U}_F$. Parameters are the same as those in Fig. 17.

Therefore, at quadratic order, Eq. (16) is

$$\frac{\partial h^{(2)}}{\partial x} Ax = Bh^{(2)}(x) + g^{(2)}(x, 0), \tag{28}$$

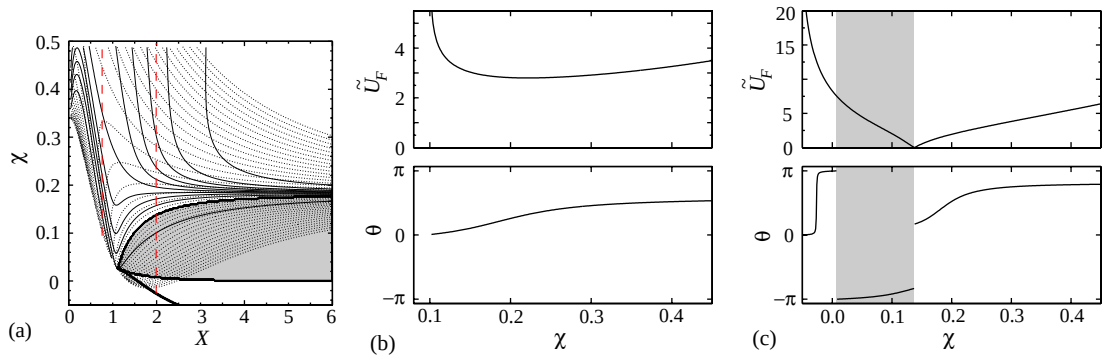


Fig. 20. Slices of data, typical in cases without divergent flutter. (a) Re-display of Fig. 18(a), showing two slices as dashed lines. Parameters are the same except: (b) $X$ is fixed at 0.75, and (c) $X$ is fixed at 2.0.

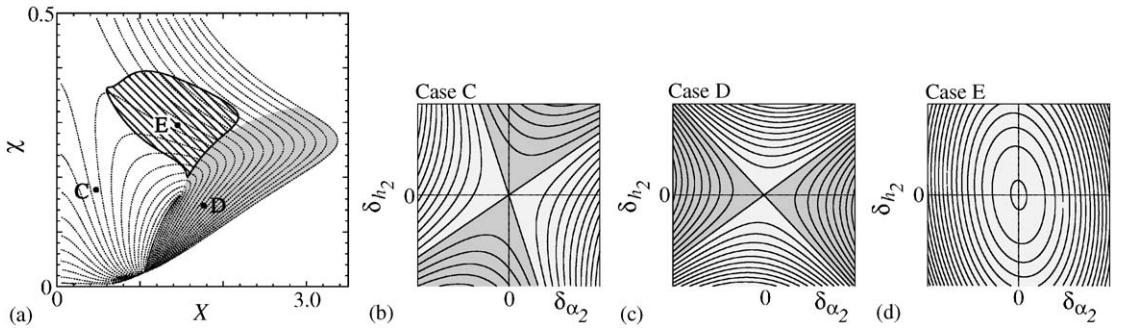


Fig. 21. For the parameters of Fig. 8, we show regions (cross-hatched) in (a) for which $c_\lambda$ in Eq. (29) is positive definite. Elsewhere it is hyperbolic. Level sets of $c_\lambda$ for the three typical cases labelled C, D, and E, respectively in (a) are shown as (b) C, (c) D and (d) E.

where $h^{(2)}(x)$ is the quadratic part of the center manifold as in Section 3.1. One can easily solve Eq. (28) for the expansion coefficients in $h^{(2)}$, which will be linear functions of the coefficients $\delta_{\alpha_2}$ and $\delta_{h_2}$. Then, in Eq. (18), we may write $f(x,h(x)) = f^{(2)}(x,0) + f^{(3)}(x,0) + f^{(2)}(x,h^{(2)}(x)) + \mathcal{O}(4)$. Here, the expansion coefficients in $f^{(2)}(x,0)$ are linear in $\delta_{h_2}$ and $\delta_{\alpha_2}$, while those of the cubic order pieces of $f^{(2)}(x,h^{(2)}(x))$ are quadratic in $\delta_{h_2}$ and $\delta_{\alpha_2}$. As before, the expansion coefficients of $f^{(3)}(x,0)$ are linear in $\delta_{h_3}$ and $\delta_{\alpha_3}$. Finally, since Eq. (21) is linear in the cubic expansion coefficients and quadratic in the quadratic expansion coefficients, we find

$$c_{\lambda_*} = d_{\alpha\alpha}\delta_{\alpha_2}^2 + d_{\alpha h}\delta_{\alpha_2}\delta_{h_2} + d_{hh}\delta_{h_2}^2 + p\delta_{\alpha_3} + q\delta_{h_3}. \tag{29}$$

Thus, the $(\delta_{\alpha_2}, \delta_{h_2}) \mapsto (-\delta_{\alpha_2}, -\delta_{h_2})$ symmetry anticipated above holds. Having investigated cubic non-linearities already, we set $\delta_{\alpha_3} = \delta_{h_3} = 0$ in Eq. (29) and consider the remaining quadratic form.

Returning to the "typical cases" of Section 4.1 with $\xi_{ea} = 0.6$, $\mu = 20$, and $r_\alpha = 0.5$, we consider three systems as labelled C, D, and E in Fig. 21(a). The shaded region corresponding to $\theta < 0$ in

Fig. 10 is transferred over to Fig. 21(a) for illustrative purposes. For system C, the quadratic form in Eq. (29) is hyperbolic: certain combinations of $\delta_{\alpha_2}$ and $\delta_{h_3}$ yield positive values of $c_{\lambda *}$ and hence subcritical Hopf bifurcations, while others cause supercritical bifurcations with $c_{\lambda *} < 0$. For system D, the quadratic form for $c_{\lambda *}$ is hyperbolic also. However, note that the roles of $\delta_{h_2}$ and $\delta_{\alpha_2}$ have been interchanged. An explanation for the reversal of roles is identical to that for the cubic coefficients provided in Section 4.4.

Finally, in system E, the quadratic form for $c_{\lambda *}$ is positive definite and the level sets are elliptic as shown in the corresponding plot. Here, any non-zero combination of $\delta_{\alpha_2}$ and $\delta_{h_2}$ causes the Hopf bifurcation to be subcritical. Such positive definite (or subcritical definite) cases persist throughout the cross-hatched region of Fig. 21(a).

For the sets of parameters used to generate Fig. 18, we provide plots for the quadratic effects, analogous to Fig. 21 in Fig. 22. Within a sea of mostly hyperbolic character for which both types of Hopf bifurcations are possible, there are islands of positive definite normal form coefficients, indicated with a cross-hatched pattern, in which the quadratic non-linearities produce only subcritical Hopf bifurcations. Interestingly, negative definite regions, in which only supercritical Hopf bifurcations occur, are rare. The only such occurrence in the systems of Fig. 22 happens in the in a very small island in the bottom right plot with $\xi_{ea} = 1.8$ and $r_\alpha = 1.2$.

## 6. Comparisons to harmonic balance

Equivalent linearization via harmonic balance, also known as the method of describing functions, has been successfully employed in the study of post-instability behavior of the flutter problem with structural non-linearities [4,10–12]. In procedures [29,30], one assumes a sinusoidal solution. Then, upon substitution into the equations of motion and truncation of higher harmonics that arise through the non-linearities, one investigates conditions under which the assumed solutions are approximately satisfied.

One of the key assumptions in the describing function approach is that the system possesses a strong filtering property which severely attenuates superharmonics. Despite claims made by Shen [10], it is not clear that the flutter problem possesses such a property. This is one of the reasons we have relied on normal forms, which have a more rigorous foundation, from which to perform analysis.

Nonetheless, the approach is not without merit. For small amplitudes, the lower harmonics do tend to dominate, and the method provides intuitively appealing explanations for the nature of the behavior. As a postscript, we shall use harmonic balance to generate $\theta$ data as in Section 4.1 and compare results with Fig. 8.

We find it simplest to perform the harmonic analysis on the dimensional version of the equations of motion

$$\begin{aligned} &m\ddot{h} - mb\chi\ddot{\alpha} + k_{h_1}h + k_{h_3}h^3 = L, \\ &-mb\chi\ddot{h} + I_{ea}\ddot{\alpha} + k_{\alpha_1}\alpha + k_{\alpha_3}\alpha^3 = M_{ea}. \end{aligned} \tag{30}$$

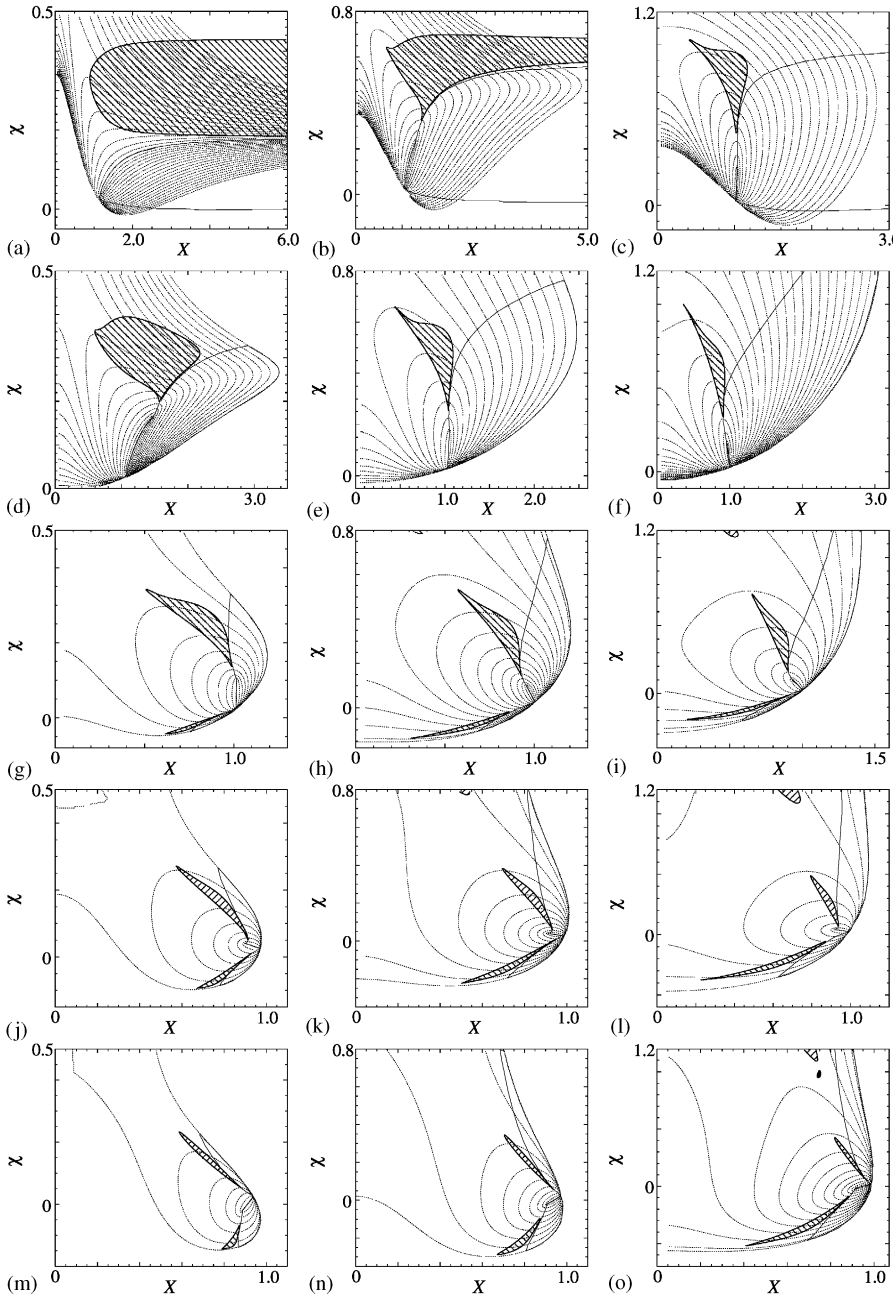


Fig. 22. Effects of quadratic non-linearities with parameters identical to those of Fig. 16. Regions for which $c_{\lambda *}$ is positive definite and negative definite are indicated by cross-hatching and solid black fill, respectively. Otherwise, the quadratic form is hyperbolic. Light shaded regions correspond to $\theta<0$ for reference. Level sets of $\tilde{U}_F$ are juxtaposed.

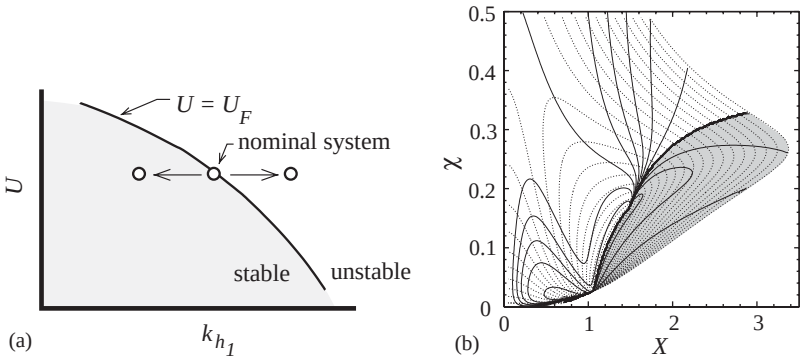


Fig. 23. (a) Consequence of changing effective spring stiffnesses. (b) Level sets of $\theta$ calculated using harmonic balance. Parameters are the same as those used in Fig. 8(a).

We start by assuming a sinusoidal solution: $h = h_1 \sin(\omega t)$, $\alpha = \alpha_1 \sin(\omega t + \phi)$. The terms $k_{h_1} h + k_{h_3} h^3$, $k_{\alpha_1} \alpha + k_{\alpha_3} \alpha^3$, representing structural restoring forces in Eq. (30) become

$$\begin{aligned} & k_{h_1} h_1 \sin(\omega t) + k_{h_3} h_1^3 \left[\tfrac{3}{4} \sin(\omega t) - \tfrac{1}{4} \sin(3\omega t)\right] \\ & \quad \rightarrow \; k_{h_1} \left[1 + \frac{3\delta_{\alpha_3}}{4} \frac{h_1^2}{b^2}\right] h_1 \sin(\omega t), \\ & k_{\alpha_1} \alpha_1 \sin(\omega + \phi) + k_{\alpha_3} \alpha_1^3 \left[\tfrac{3}{4} \sin(\omega t + \phi) - \tfrac{1}{4} \sin(3\omega t + 3\phi)\right] \\ & \quad \rightarrow \; k_{\alpha_1} \left[1 + \frac{3\delta_{\alpha_3}}{4} \alpha_1^2\right] \alpha_1 \sin(\omega t + \phi), \end{aligned} \tag{31}$$

respectively. The right arrows ($\rightarrow$) above filter out the leading harmonic and make connections to the dimensionless cubic coefficients $\delta_{*_3}$. From the perspective of harmonic balance, the cubic non-linearities effectively augment the linear plunge and pitch spring stiffnesses by $k_{h_1} \delta_{h_3} 3h_1^2/4b^2$ and $k_{\alpha_1} \delta_{\alpha_3} 3\alpha_1/4$, respectively. The amounts by which the stiffnesses change are proportional the cubic coefficients $\delta_{\alpha_3}$, $\delta_{h_3}$, and to the square of the oscillation amplitudes.

In Fig. 23(a), we show a schematic plot of $U_F$, the flutter velocity of the linearized system, as a function of plunge spring stiffness, $k_{h_1}$. All other parameters are held fixed. Consider a nominal system with parameters chosen so that it lies directly on the stability boundary as depicted in Fig. 23(a). Then, as one perturbs the oscillation amplitude from zero, the effective plunge spring stiffness either increases or decreases, depending on the sign of $\delta_{h_3}$. If $\delta_{h_3} > 0$, the spring effectively gets stiffer with increasing amplitude, and from the perspective of the first harmonic, the system is drawn into the unstable regime where solutions grow. Therefore, the $\delta_{h_3} > 0$ non-linearity induces growth of solutions in Fig. 23(a), similar to systems exhibiting subcritical Hopf bifurcations. Likewise, $\delta_{h_3} < 0$ shows characteristics of supercritical bifurcations.

The boundary between subcritical and supercritical bifurcations in Fig. 7 corresponds to combinations of $\delta_{\alpha_3}$ and $\delta_{h_3}$ that leaves $c_{\lambda *}$ fixed at zero. From the harmonic balance perspective, the boundary coincides with combinations of $\delta_{\alpha_3}$ and $\delta_{h_3}$ (or $k_{\alpha_3}$ and $k_{h_3}$) that leaves $U$ fixed at $U_F$.

To express this mathematically, let $p(\lambda)$ denote the characteristic polynomial of the linearized system; then define $p_r(\Omega)$ and $p_i(\Omega)$ to be the real and imaginary parts, respectively of $p(\mathrm{i}\Omega)$. If

$\lambda = \mathrm{i}\omega$ is an eigenvalue of the nominal system, then $p(\mathrm{i}\omega) = p_r(\omega) = p_i(\omega) = 0$. Taking differentials, we obtain

$$\left.\frac{\partial p_r}{\partial \Omega}\right|_0 \mathrm{d}\Omega + \left.\frac{\partial p_r}{\partial k_{\alpha_1}}\right|_0 \mathrm{d}k_{\alpha_1} + \left.\frac{\partial p_r}{\partial k_{h_1}}\right|_0 \mathrm{d}k_{h_1} + \left.\frac{\partial p_r}{\partial U}\right|_0 \mathrm{d}U = 0,$$
$$\left.\frac{\partial p_i}{\partial \Omega}\right|_0 \mathrm{d}\Omega + \left.\frac{\partial p_i}{\partial k_{\alpha_1}}\right|_0 \mathrm{d}k_{\alpha_1} + \left.\frac{\partial p_i}{\partial k_{h_1}}\right|_0 \mathrm{d}k_{h_1} + \left.\frac{\partial p_i}{\partial U}\right|_0 \mathrm{d}U = 0. \tag{32}$$

The derivatives are evaluated for $\Omega = \omega$, $U = U_F$, and all other parameters set to those corresponding to the nominal system at criticality. We set $\mathrm{d}U = 0$ so that $U$ remains constant at $U = U_F$ as described above. Eliminating $\mathrm{d}\Omega$ from Eq. (32), expressing $k_{\alpha_1}$ and $k_{h_1}$ in terms of $\delta_{\alpha_1}$ and $\delta_{h_1}$ as discussed above, and setting $\alpha_1 = \beta h_1$, we obtain

$$\frac{\delta_{h_1}}{\delta_{\alpha_1}} = \frac{r_\alpha^2 b^2 \beta^2}{X^2}\left[\frac{\left.\frac{\partial p_i}{\partial k_{\alpha_1}}\right|_0 - \left.\frac{\partial p_r}{\partial k_{\alpha_1}}\right|_0}{\left.\frac{\partial p_r}{\partial k_{h_1}}\right|_0 - \left.\frac{\partial p_i}{\partial k_{h_1}}\right|_0}\right]. \tag{33}$$

The quantity $\beta$ may be obtained from the critical eigenvector. The portion above in square brackets has units $1/\mathrm{length}^2$, and the entire right hand side of Eq. (33) may be expressed in terms of the dimensionless quantities used throughout the paper. Although the expression is lengthy, consuming several pages, it is manageable using symbolic mathematics software. Taking the arctangent of Eq. (33) yields the angle $\theta$ in Fig. 7.

For comparison, we return once again to the typical system of Section 4.1. Using the range of parameters outlined there, we compute $\theta$ using Eq. (33), shade the region with $\theta < 0$, and superimpose level sets of $\tilde{U}_F$. The plot is shown in Fig. 23(b). The results are indistinguishable from those computed via normal forms in Fig. 8(a). We have obtained similar corroborating results for other sets of parameter values and for quadratic non-linearities. The time to compute the $\theta$ data in Fig. 23(b) is roughly the same as that required to compute Fig. 8(a). The most time-consuming part of the computation are the eigenvalue/eigenvector calculations necessary in both approaches.

## 7. Conclusions

Although the data are cumbersome to display, the normal form approach promoted here is effective and efficient at performing extensive parametric studies of the non-linear character of the flutter Hopf bifurcation. In performing such an analysis, we find that counterexamples to the flutter criticality hypothesis are far more common than expected, based upon the literature over the past half-century. Perhaps the lack of counterexamples is largely due to the fact that they typically occur for $X > 1$, outside what are usually regarded as practically relevant systems.

However, one of our primary motivations for this study comes from a class of flow separation problems in which it has been demonstrated that small amplitude, open-loop, periodic perturbations have been shown to dramatically improve performance measures: e.g., lift enhancement, pressure recovery, or drag reduction. The work reported here is part of a larger

effort to explore the possibility of using small fluttering airfoils as semi-passive flow actuators in such applications. In this context, aeroelastic systems for which $X > 1$ are relevant.

Furthermore, it is within this context that the normal form approach developed herein truly demonstrates its utility. Not only do normal forms provide an efficient framework for performing parametric qualitative studies of non-linear dynamics, the approach naturally extends to the study of multiple interacting aeroelastic instabilities as we demonstrate in the companion papers [14,31]. Describing functions are not suitable in such situations. Bifurcation-tracking and continuation software packages such as AUTO [21] and CONTENT [22] are far less efficient in large scale parametric explorations.

It is worth noting, however, that the normal form approach advocated herein does not provide detailed information about dependence on initial conditions, as does direct numerical simulation. In this sense, our work is complementary to traditional approaches.

## Acknowledgements

We wish to acknowledge the contribution of Daniel Neidlinger and Marina Tharayil who performed some of the earlier analyses as part of their undergraduate research projects.

## Appendix A. Nomenclature

| | |
|---|---|
| $h$ | vertical displacement of elastic axis (positive upward) |
| $\alpha$ | airfoil pitch (positive nose up) |
| $t$ | time |
| $b$ | half the airfoil's chord |
| $\rho$ | fluid density per unit depth |
| $m$ | mass of airfoil |
| $I_{ea}$ | moment of inertia about elastic axis |
| $-[k_{h_1}h + k_{h_2}h^2 + k_{h_3}h^3]$ | restoring force of plunge spring |
| $-[k_{\alpha_1}\alpha + k_{\alpha_2}\alpha^2 + k_{\alpha_3}\alpha^3]$ | restoring force of pitch spring |
| $\omega_h$ | uncoupled natural plunge frequency $\left(=\sqrt{k_{h_1}/m}\right)$ |
| $\omega_\alpha$ | uncoupled natural pitch frequency $\left(=\sqrt{k_{\alpha_1}/I_{ea}}\right)$ |
| $V$ | potential function for restoring forces |
| $L$ | aerodynamic lift |
| $M_{ea}$ | aerodynamic moment about elastic axis |

*Dimensionless parameters*

| | |
|---|---|
| $\tilde{h}$ | normalized displacement airfoil displacement $(= h/b)$ |
| $\chi b$ | location of center of mass of airfoil aft of the elastic axis |
| $\xi_{ea} b$ | location of the elastic axis aft of the leading edge |
| $\tau$ | dimensionless time $(= \omega_\alpha t)$ |
| $\delta_{h_2}$ | quadratic plunge spring coefficient $(= bk_{h_2}/k_{h_1})$ |

| | |
|---|---|
| $\delta_{h_3}$ | cubic plunge spring coefficient ($= b^2 k_{h_3}/k_{h_1}$) |
| $\delta_{\alpha_2}$ | quadratic pitch spring coefficient ($= k_{\alpha_2}/k_{\alpha_1}$) |
| $\delta_{\alpha_3}$ | cubic pitch spring coefficient ($= k_{\alpha_3}/k_{\alpha_1}$) |
| $X$ | ratio of uncoupled natural frequencies ($= \omega_h/\omega_\alpha$) |
| $\mu$ | mass ratio ($= m/\pi\rho b^2$) |
| $r_\alpha$ | dimensionless radius of gyration ($= I_{ea}/mb^2$) |
| $\tilde{V}$ | dimensionless potential ($= V/k_{\alpha_1}$) |
| $\tilde{U}$ | dimensionless flow speed ($= U/b\omega_\alpha$) |
| $\tilde{L}$ | dimensionless lift ($= L/\pi\rho b U^2$) |
| $\tilde{M}_{ea}$ | dimensionless moment about elastic axis ($= M_{ea}/\pi\rho U^2$) |
| $K_j$ | coefficients in exponential approximation of Wagner's function |
| $\sigma_j$ | exponents in exponential approximation of Wagner's function |

## References

[1] J.E. Marsden, M. McCracken, *The Hopf Bifurcation and its Applications*, Springer, Berlin, 1976.
[2] D.S. Woolston, H.L. Runyan, R.E. Andrews, An investigation of effects of certain types of structural nonlinearities on wing and control surface flutter, *Journal of the Aeronautical Sciences* 24 (1957) 57–63.
[3] B.H.K. Lee, L.Y. Jiang, Y.S. Wong, Flutter of an airfoil with cubic restoring force, *Journal of Fluids and Structures* 13 (1999) 75–101.
[4] S.J. Price, H. Alighanbari, B.H.K. Lee, The aeroelastic response of a 2-dimensional airfoil with bilinear and cubic structural nonlinearities, *Journal of Fluids and Structures* 9 (1995) 175–193.
[5] H. Alighanbari, S.J. Price, The post-Hopf-bifurcation response of an airfoil in incompressible two-dimensional flow, *Nonlinear Dynamics* 10 (4) (1996) 381–400.
[6] B.H.K. Lee, S.J. Price, Y.S. Wong, Nonlinear aeroelastic analysis of airfoils: bifurcation and chaos, *Progress in Aerospace Sciences* 35 (3) (1999) 205–334.
[7] L.N. Virgin, E.H. Dowell, M.D. Conner, On the evolution of deterministic non-periodic behavior of an airfoil, *International Journal of Non-linear Mechanics* 34 (3) (1999) 499–514.
[8] B.D. Coller, P. Holmes, J.L. Lumley, Suppression of bursting, *Automatica* 33 (1997) 1–11.
[9] A. Raghothama, S. Narayanan, Non-linear dynamics of a two-dimensional airfoil by incremental harmonic balance method, *Journal of Sound and Vibration* 226 (3) (1999) 493–517.
[10] S.F. Shen, An approximate analysis of nonlinear flutter problems, *Journal of the Aerospace Sciences* 26 (1) (1959) 25–32,45.
[11] D.M. Tang, E.H. Dowell, Flutter and stall response of a helicopter blade with structural nonlinearity, *Journal of Aircraft* 29 (5) (1992) 953–960.
[12] Z.C. Yang, L.C. Zhao, Analysis of limit-cycle flutter of an airfoil in incompressible flow, *Journal of Sound and Vibration* 123 (1) (1988) 1–13.
[13] P.A. Chamara, B.D. Coller, Double flutter in an aeroelastic system, *American Institute of Aeronautics and Astronautics Journal* 39 (6) (2000) 1206–1208.
[14] P.A. Chamara, B.D. Coller, A study of double flutter, *Journal of Fluids and Structures* 19 (7) (2004) 863–879.
[15] L. Liu, Y.S. Wong, B.H.K. Lee, Application of the centre manifold theory in non-linear aeroelasticity, *Journal of Sound and Vibration* 234 (4) (2000) 641–659.
[16] Y.C. Fung, *An Introduction to the Theory of Aeroelasticity*, Dover, New York, 1993.
[17] R.T. Jones, The unsteady lift of a wing of finite aspect ratio, Technical Report 681, NACA Report, 1940.
[18] W.P. Jones, Aerodynamic forces on wings in non-uniform motion, Technical Report 2117, Aeronautical Research Council R. & M., 1945.
[19] J. Guckenheimer, P.J. Holmes, *Nonlinear Oscillations, Dynamical Systems and Bifurcations of Vector Fields*, Springer, Berlin, 1983.

[20] S. Wiggins, *Introduction to Applied Nonlinear Dynamical Systems and Chaos*, Springer, Berlin, 1990.
[21] E. Doedel, A.R. Champneys, T.F. Fairgrieve, Y. Kuznetsov, B. Sandstede, X. Wang, AUTO 97: continuation and bifurcation software for ordinary differential equations, Technical Report, Concordia University, 1998.
[22] Y.A. Kuznetsov, *Elements of Applied Bifurcation Theory*, Springer, Berlin, 1998.
[23] B.D. Coller, Intriguing nonlinear phenomena associated with actuator-induced instabilities, *Automatica*, in press.
[24] R.L. Bisplinghoff, A. Holt, R.L. Halfman, *Aeroelasticity*, Addison-Wesley, Reading, MA, 1957.
[25] M.J. Kim, D.T. Mook, Application of continuous vorticity panels to general unsteady incompressible two-dimensional lifting flows, *Journal of Aircraft* 23 (1985) 464–471.
[26] K.C. Hall, Eigenanalysis of unsteady flows about airfoils, cascades, and wings, *American Institute of Aeronautics and Astronautics Journal* 32 (1994) 2426–2432.
[27] A.M. Kuethe, Y.C. Chow, *Foundations of Aerodynamics: Bases of Aerodynamic Design*, Wiley, New York, 1986.
[28] M.A. Biot, L. Arnold, Low speed flutter and its physical interpretation, *Journal of the Aeronautical Sciences* 15 (4) (1948) 232–236.
[29] N. Minorsky, *Nonlinear Oscillations*, Van Nostrand, Princeton, NJ, 1962.
[30] H.K. Khalil, *Nonlinear Systems*, Prentice-Hall, Englewood Cliffs, NJ, 1995.
[31] P.A. Chamara, B.D. Coller, Subcritical/supercritical cascade flutter and simplifying effects of symmetry, Technical Report DSCL 01-02, Northern Illinois University, 2001, *Journal of Fluids and Structures*, submitted.